iScience

CellPress
OPEN ACCESS

Article

Azathioprine antagonizes aberrantly elevated lipid metabolism and induces apoptosis in glioblastoma

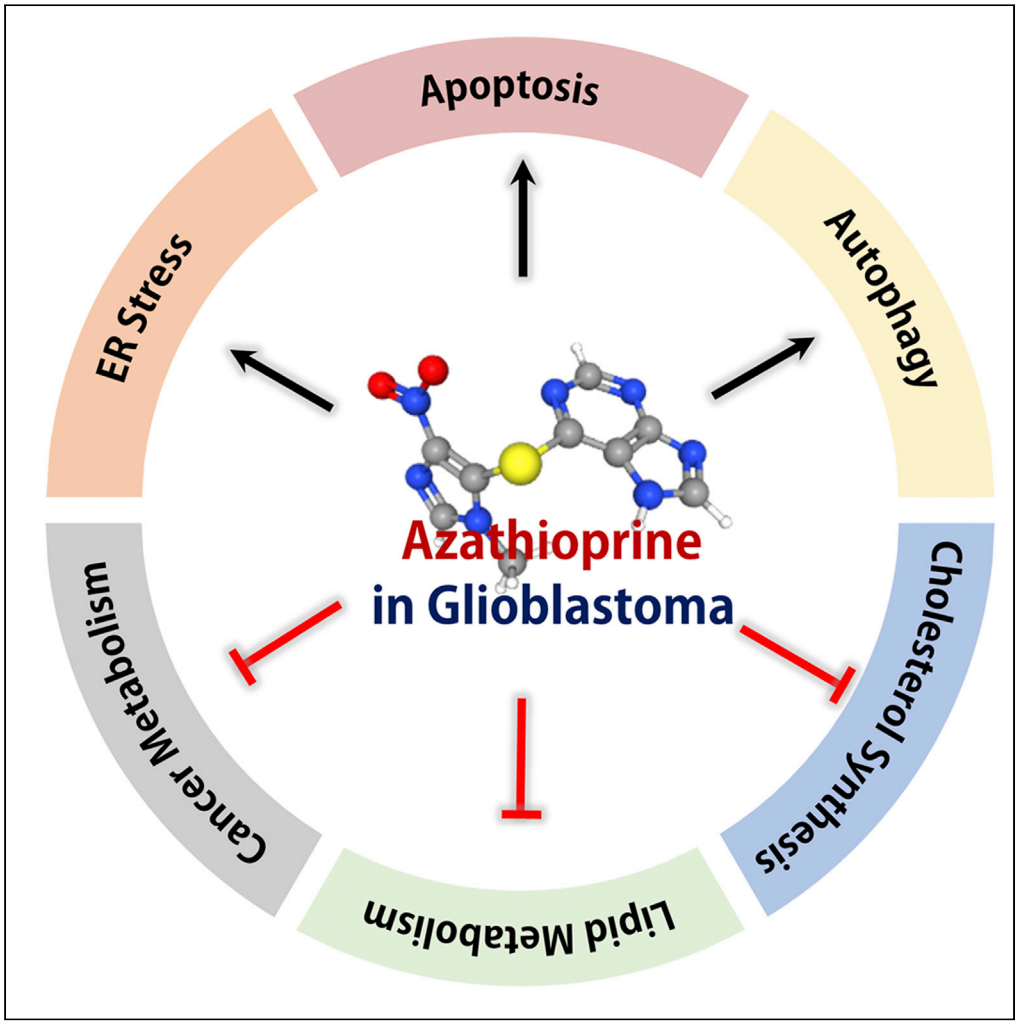

Hye Jin Nam, Young Eun Kim, Byoung-San Moon, ..., Jeong Woon Jang, Do-Hyun Nam, Heeyeong Cho

hycho@krict.re.kr

HIGHLIGHTS

Azathioprine as a promising drug for temozolomide-resistant GBM treatment

Azathioprine inhibits aberrantly elevated lipid metabolism in GBM

Azathioprine promotes ER stress-induced apoptosis in GBM

Through orthotropic xenograft models, anti-GBM effect of azathioprine is confirmed

Nam et al., iScience *24*, 102238
March 19, 2021
https://doi.org/10.1016/j.isci.2021.102238

iScience

CellPress
OPEN ACCESS

Article

Azathioprine antagonizes aberrantly elevated lipid metabolism and induces apoptosis in glioblastoma

Hye Jin Nam,[1] Young Eun Kim,[1] Byoung-San Moon,[2] Hyun Young Kim,[1] Daeyoung Jung,[1] Seungho Choi,[1] Jeong Woon Jang,[1] Do-Hyun Nam,[3] and Heeyeong Cho[1,4,*]

SUMMARY

Glioblastoma multiforme (GBM) is the most aggressive type of brain tumor with poor survival rate. Temozolomide (TMZ) is used as standard chemotherapy to treat GBM, but a large number of patients either respond poorly and/or develop resistance after long-term use, emphasizing the need to develop potent drugs with novel mechanisms of action. Here, using high-throughput compound screening (HTS), we found that azathioprine, an immunosuppressant, is a promising therapeutic agent to treat TMZ-resistant GBM. Through integrative genome-wide analysis and global proteomic analysis, we found that elevated lipid metabolism likely due to hyperactive EGFR/AKT/SREBP-1 signaling was inhibited by azathioprine. Azathioprine also promoted ER stress-induced apoptosis. Analysis of orthotopic xenograft models injected with patient-derived GBM cells revealed reduced tumor volume and increased apoptosis after azathioprine and TMZ co-treatment. These data indicate that azathioprine could be a powerful therapeutic option for TMZ-resistant GBM patients.

INTRODUCTION

Glioblastoma multiforme (GBM) is the most prevalent and aggressive brain tumor and one of the most lethal of all cancers (Joo et al., 2013). GBM cells tend to invade the surrounding brain, making complete surgical excision impossible, whereas resistance to chemotherapy and radiation also contributes to poor prognosis of GBM (Joo et al., 2013). The standard therapy for GBM is surgical removal of the tumor and chemotherapy with temozolomide (TMZ) (Stupp et al., 2007). TMZ is an oral alkylating agent rapidly absorbed and spontaneously converted to the active metabolite, 3-methyl-(triazen-1-yl)imidazole-4-carboxamide (MTIC) (Baker et al., 1999). Although TMZ has been the standard chemotherapy for GBM treatment for decades, more than 50% of patients treated do not respond to TMZ, and sensitive patients eventually develop resistance (Mansouri et al., 2019). The major cause of TMZ resistance is high expression of O_6-methylguanine-DNA-methyltransferase (MGMT), which removes the cytotoxic O_6-methylguanine (O_6MG) DNA lesions created by TMZ (Mansouri et al., 2019). Despite intensive standard treatments, the median survival of GBM patients is less than 15 months (Tamimi and Juweid, 2017). GBMs show various genetic alterations along with phenotypic diversity contributing to dysregulation of numerous pathways (Meyer et al., 2015). Efforts have been made to develop novel drugs such as anti-angiogenic reagents, phosphoinositide 3-kinase (PI3K) and mTOR inhibitors, and epidermal growth factor receptor (EGFR) inhibitors (Alphandéry, 2018). Nonetheless, there remains an urgent need for effective drugs that exhibit novel mechanisms of action.

Cancer cells meet the high-energy demands of rapid proliferation using aberrant and reprogrammed metabolism (Hanahan and Weinberg, 2011). A representative metabolic feature of cancer cells is the Warburg effect, a phenomenon in which cancer cells favor glycolysis over the oxidative phosphorylation (OXPHOS) pathway, even under sufficient oxygen supply (Cantor and Sabatini, 2012). Cancer cells also show elevated lipogenesis, a characteristic directly correlated with enhanced glucose and glutamine metabolism (Gimple et al., 2019; Zou et al., 2019). GBM cells tend to show enhanced *de novo* lipid biosynthesis and utilize exogenous lipids to fuel growth, and lipid droplets can be detected in GBMs but not in low-grade gliomas or normal brain tissues (Shimano and Sato, 2017). EGFR/PI3K/AKT signaling regulates lipid metabolic reprogramming in GBM by upregulating sterol regulatory element-binding protein 1 (SREBP-1)

[1]Drug Discovery Platform Research Center, Therapeutics and Biotechnology Division, Korea Research Institute of Chemical Technology, Daejeon 34114, Republic of Korea

[2]Department of Biotechnology, Chonnam National University, Yeosu 59626, Republic of Korea

[3]Department of Neurosurgery, Samsung Medical Center (SMC), Sungkyunkwan University School of Medicine, Seoul 06351, Republic of Korea

[4]Lead contact

*Correspondence: hycho@krict.re.kr

https://doi.org/10.1016/j.isci.2021.102238

transcriptional activity (Guo et al., 2009; Oishi et al., 2017; Shimano and Sato, 2017). Inhibition of that activity significantly induces GBM cell death, indicating that SREBP-1 is a promising target in GBM (Cheng et al., 2018a, 2018b; Guo et al., 2014). In addition, because rewired metabolism is considered a primary cause of chemoresistance (Rahman and Hasan, 2015), targeting altered metabolism has emerged as a promising strategy to improve overall survival of GBM patients.

The immunosuppressant azathioprine is widely used to prevent organ rejection following kidney and heart transplantation (Karran and Attard, 2008). Although azathioprine has been in clinical use for a long time, its precise mechanisms of action are still unclear. Recent work suggests that it inhibits *de novo* purine nucleotide synthesis as its major therapeutic mechanism (Karran and Attard, 2008).

Here, to identify new compounds to treat GBM, we performed high-throughput screening of clinical collection libraries. That analysis identified azathioprine as a promising compound for GBM treatment. Specifically, using integrative genome-wide analysis and global proteomic analysis, we showed that azathioprine antagonizes aberrantly elevated lipid metabolism and causes ER stress-induced apoptosis. In addition, experiments performed in an orthotopic model of GBM confirmed azathioprine efficacy *in vivo*. Overall, we propose azathioprine as a candidate for GBM treatment and that combinatorial treatment with TMZ could be a promising therapeutic strategy for TMZ-resistant GBM patients.

RESULTS

The landscape of somatic mutations in TMZ-resistant GBM

Based on transcriptional features, GBMs are sub-classified into four subtypes: proneural, neural, classical, and mesenchymal (Verhaak et al., 2010). Among them, proneural and mesenchymal subtypes display distinct features and aggressive phenotypes with poor prognosis (Verhaak et al., 2010). We obtained two types of cells, 559T, a proneural subtype, and 592T, a mesenchymal subtype, from TMZ-resistant patients, as well as 626T cells, a classical subtype from TMZ-sensitive patients (Oh et al., 2014). We previously reported that 559T and 592T cells exhibit an unmethylated MGMT promoter and show TMZ resistance, whereas the MGMT promoter in 626T cells was methylated (Oh et al., 2014). To confirm that promoter methylation status reflects expression levels, we examined MGMT mRNA and protein levels in all three GBM lines. As expected, MGMT mRNA and protein expression levels were dramatically elevated in 559T and 592T relative to 626T cells (Figures 1A and 1B). Based on previous work (Oh et al., 2014), we concluded that high MGMT expression is likely the primary cause of TMZ resistance in 559T and 592T cells.

To further define their genomic status, we performed whole-exome sequencing of both TMZ-resistant GBM lines. We detected a variety of exon variants in both 559T and 592T GBM cells (Figure 1C). 559T and 592T cells exhibited identical intron variants at the MGMT locus, but we detected no exon variants. Overall, we assessed mutations based on the degree of deleteriousness: start or stop gains/losses, frame shifts, exon loss, or splice donor/acceptor variants were defined as high-impact, whereas missense variants or in-frame insertions/deletions were evaluated as moderate-impact mutations. Non-coding variants or synonymous variants were not assessed. We then performed KEGG pathway analysis using a pool of high- and moderate-impact genes mutated in both 559T and 592T cells. Interestingly, the top five KEGG pathways were metabolic pathways, olfactory transduction, HSV1 infection, ECM-receptor interaction, and human papillomavirus infection (Figure 1D). The most notable mutations in genes functioning in metabolic pathways were HK1 (H7R) and HK2 (R844K), which are the first enzymes in the glycolysis pathway. Genes encoding the gluconeogenesis regulatory enzymes FBP1 (R218K) and FBP2 (V86L) were also mutated in 559T and 592T cells. Several genes of the aldehyde dehydrogenase family, namely ALDH1B1 (V253M), ALDH3B1 (frameshift in S78, V301, and K459) and ALDH3B2 (H361R, S220G, H203R, and S52N), were also mutated. In addition, multiple genes participating in lipid and cholesterol metabolic pathways including ABCA1 (K1587R, I883L, R219K), LIPC (N215S, F356L), LIPG (T111I), APOB (P2739L, I2313V, Y1422C, and A618V), NPC1 (I858V, M642I, and H215R), and PCSK9 (V474I, G670E) were mutated in GBM cells (Data accession code: GSE153908).

Post-replicative DNA mismatch repair (MMR) is involved by a large protein complex containing MutL homolog 1 (MLH1), MutS homolog 2 (MSH2), MutS homolog 6 (MSH6), PMS1 homolog 2 (PMS2), and exonuclease1 (EXO1) (Harfe and Jinks-Robertson, 2000). Loss of MMR activity is associated with tumor development and microsatellite genomic instability (Jiricny and Nystrom-Lahti, 2000). In addition, MMR deficiency reportedly confers a 100-fold increase in resistance to TMZ (Germano et al., 2018). We therefore

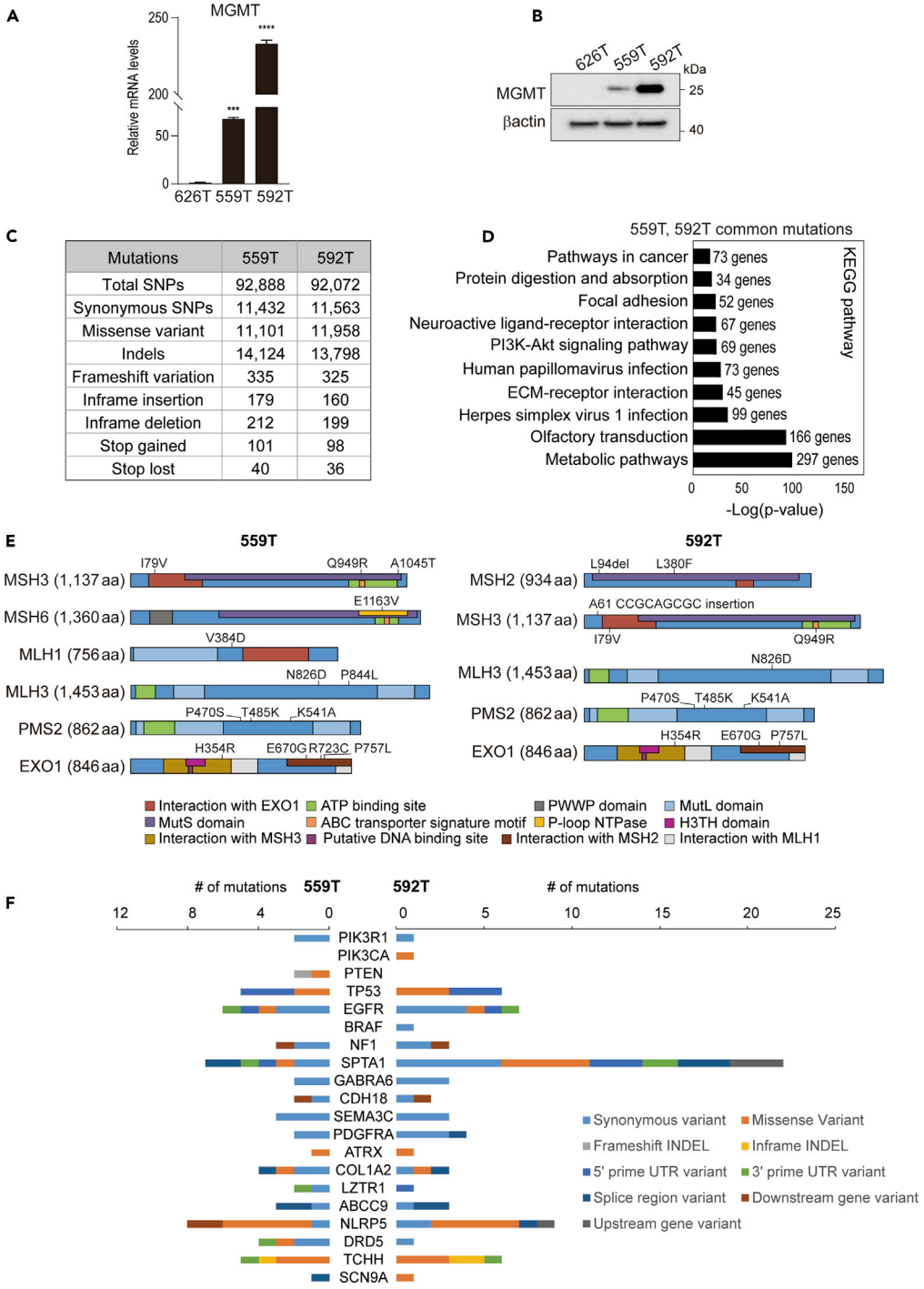

Mutations	559T	592T
Total SNPs	92,888	92,072
Synonymous SNPs	11,432	11,563
Missense variant	11,101	11,958
Indels	14,124	13,798
Frameshift variation	335	325
Inframe insertion	179	160
Inframe deletion	212	199
Stop gained	101	98
Stop lost	40	36

Figure 1. Somatic mutation profiling of patient-derived GBM cells

(A and B) Quantitative RT-PCR analysis (A) and immunoblot analysis (B) of GBM cells to detect MGMT expression levels. Data are expressed as mean ± SD; n = 3. ***$p < 0.0001$, ****$p < 0.0001$ (unpaired t test versus 626T).

(C) Summary of total somatic mutations in 559T and 592T cells.

(D) KEGG analysis using common mutations seen in 559T and 592T. Among them, mutations with high or moderate impact were used for the analysis.

(E) Schematic showing missense mutations seen in 559T and 592T involving proteins associated with MMR.

(F) Somatic mutations seen in 559T and 592T cells in genes previously reported as significantly associated with GBM.

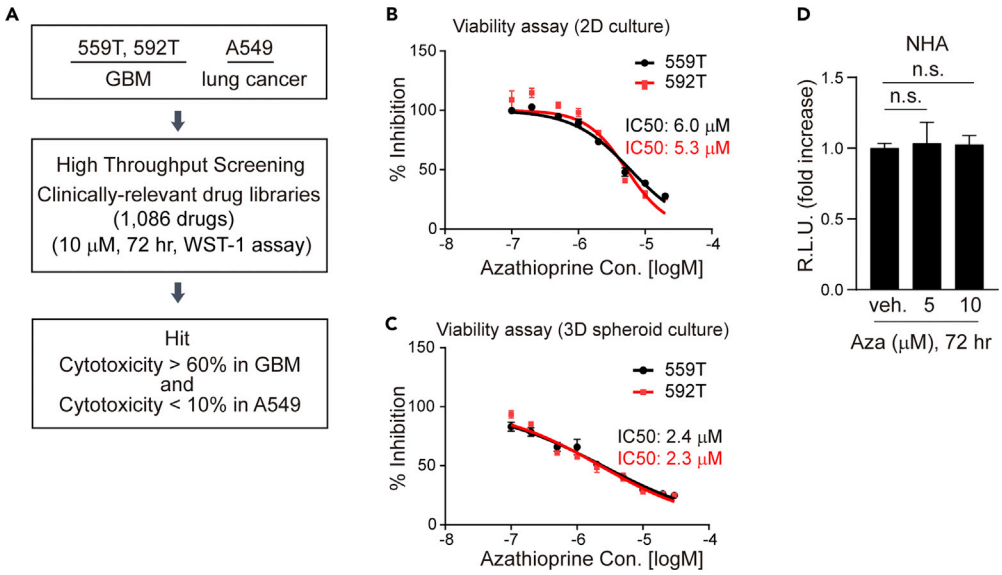

Figure 2. Azathioprine has dramatic anti-cancer effects against GBM cells but not normal astrocytes

(A) Flow chart showing high-throughput screening strategy. Cell cytotoxicity was assessed using a WST-1 kit. Experiments were performed in triplicate.

(B–D) 2D viability assay using a CCK-8 kit (B) or a 3D viability assay with the CellTiter-Glo 3D cell viability kit (C and D). Both assays were performed after treatment with serially diluted azathioprine for 72 h. NHA, normal human astrocyte. R.L.U., relative luciferase units. Dose-response curve fitting used nonlinear regression (B and C). Data are expressed as mean ± SD; n = 3. DMSO served as vehicle.

See also Table S1.

investigated potential mutations in components of the MMR complex. Interestingly, 559T and 592T cells harbored numerous missense mutations within important functional domains of MMR proteins (Figure 1E). In particular, the MSH3 mutation I79V is within the domain required for interaction with EXO1. Surprisingly, EXO1 also showed mutations within domains important for its interaction with MSH3 or MSH2. These findings suggest that mutations in MMR components combined with high MGMT expression may contribute to TMZ resistance in these cell types.

We also analyzed genes commonly mutated in GBM (Figure 1F) (Brennan et al., 2013). A frameshift deletion in the PTEN tumor suppressor and gain-of-function mutation in the DNA-binding domain of TP53 (R248Q) were seen in 559T cells (Olivier et al., 2010). Interestingly, a TP53 mutation (P72R) associated with lipid accumulation and metabolic dysfunction (Kung et al., 2016) was found in both 559T and 592T cells. Overall, we conclude that somatic mutations in critical hotspot genes contribute to metabolic reprogramming and chemotherapy resistance in GBM.

Identification of azathioprine as a potential drug against GBM

To identify novel drugs useful to treat TMZ-resistant GBM, we undertook a high-throughput screen using a clinical collection library (1,086 drugs) and performed that screen in 559T and 592T cells (Figure 2A). To assess whether cell death was GBM-specific, we used the lung cancer A549 cell line for comparison. That analysis identified azathioprine and dofetilide as hit molecules with GBM-specific potent efficacy (Table S1). Immunosuppressive azathioprine is widely used following organ transplantation and has an antiproliferative effect on lymphocytes (Wang et al., 2017). After absorption by the body, azathioprine is converted to a purine analog and inhibits purine synthesis (Karran and Attard, 2008). Interestingly, purine synthesis is essential for maintenance of brain tumor initiating cells (BTICs) (Wang et al., 2017). Based on these observations, we focused our analysis on azathioprine.

To confirm its efficacy against GBM, we treated 559T and 592T cells with azathioprine at various concentrations. Half maximal inhibitory concentrations were similar in 559T (IC50: 6.0 μM) and 592T (IC50: 5.3 μM) lines (Figure 2B). Normally, 559T and 592T cells are cultured in suspension and are predominantly spherical.

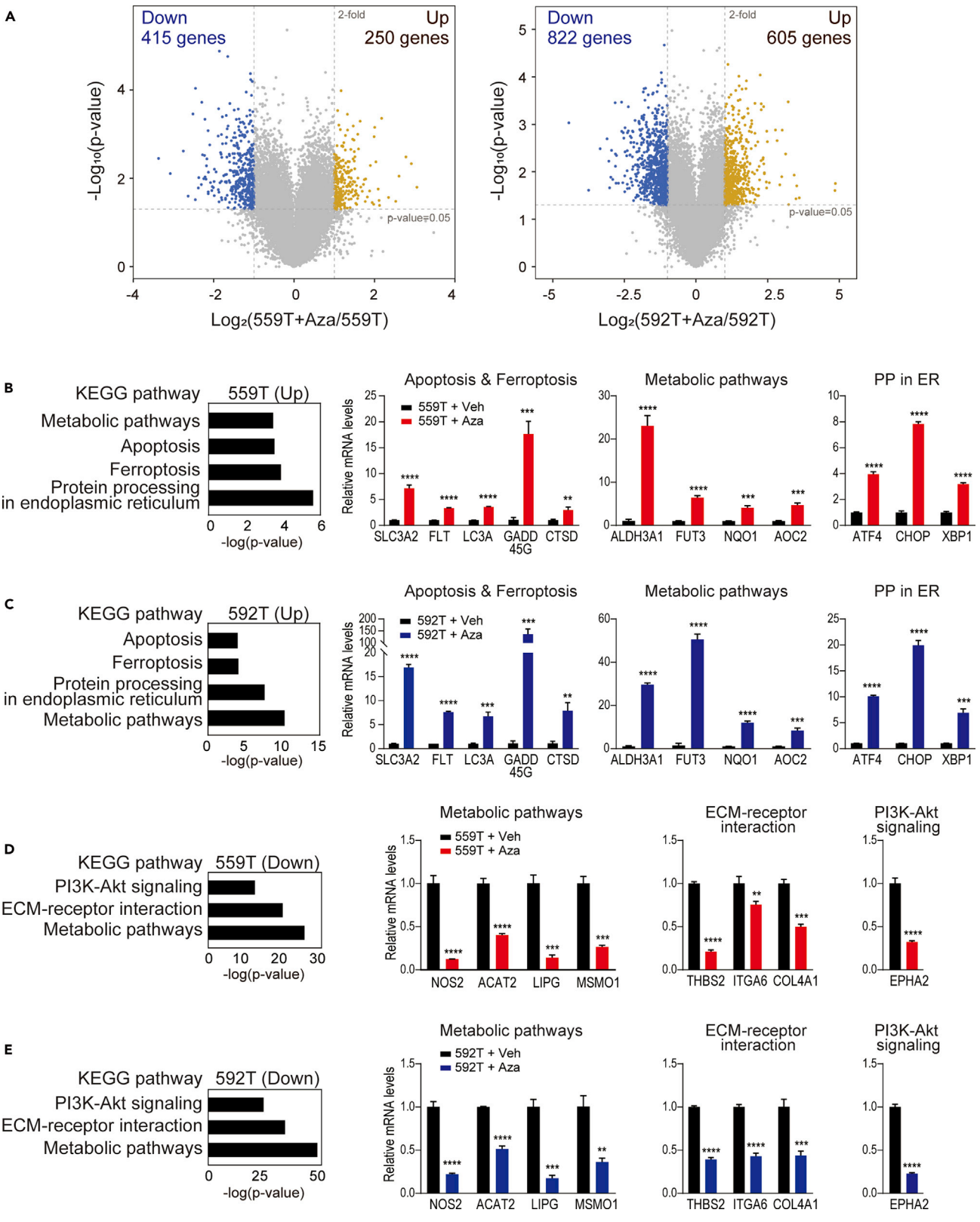
A
Down
415 genes
2-fold
Up
250 genes
p-value=0.05
-Log10(p-value)
Log2(559T+Aza/559T)
Down
822 genes
2-fold
Up
605 genes
p-value=0.05
-Log10(p-value)
Log2(592T+Aza/592T)
B
KEGG pathway
559T (Up)
Metabolic pathways
Apoptosis
Ferroptosis
Protein processing in endoplasmic reticulum
-log(p-value)
Apoptosis & Ferroptosis
559T + Veh
559T + Aza
Relative mRNA levels
SLC3A2
FLT
LC3A
GADD 45G
CTSD
Metabolic pathways
ALDH3A1
FUT3
NQO1
AOC2
PP in ER
ATF4
CHOP
XBP1
C
KEGG pathway
592T (Up)
Apoptosis
Ferroptosis
Protein processing in endoplasmic reticulum
Metabolic pathways
-log(p-value)
Apoptosis & Ferroptosis
592T + Veh
592T + Aza
Relative mRNA levels
SLC3A2
FLT
LC3A
GADD 45G
CTSD
Metabolic pathways
ALDH3A1
FUT3
NQO1
AOC2
PP in ER
ATF4
CHOP
XBP1
D
KEGG pathway
559T (Down)
PI3K-Akt signaling
ECM-receptor interaction
Metabolic pathways
-log(p-value)
Metabolic pathways
559T + Veh
559T + Aza
Relative mRNA levels
NOS2
ACAT2
LIPG
MSMO1
ECM-receptor interaction
THBS2
ITGA6
COL4A1
PI3K-Akt signaling
EPHA2
E
KEGG pathway
592T (Down)
PI3K-Akt signaling
ECM-receptor interaction
Metabolic pathways
-log(p-value)
Metabolic pathways
592T + Veh
592T + Aza
Relative mRNA levels
NOS2
ACAT2
LIPG
MSMO1
ECM-receptor interaction
THBS2
ITGA6
COL4A1
PI3K-Akt signaling
EPHA2

Figure 3. mRNA-sequencing analysis reveals regulation of several cancer-associated pathways by azathioprine

(A–E) 559T or 592T cells were treated with 10 μM azathioprine or DMSO vehicle for 48 h for mRNA-sequencing analysis. (A) Volcano plots displaying $\log_2$ fold-change (azathioprine treatment/control groups) against the -$\log_{10}$ (p value) in 559T (left) and 592T (right) cells. Gray dashed lines indicate the significance threshold (fold-change = 2, p value = 0.05). Differentially downregulated genes are highlighted by blue dots and upregulated by yellow dots. (B–E) KEGG pathway analysis using up- (B, C) or downregulated (D, E) gene pools in 559T or 592T cells. Quantitative RT-PCR analysis was conducted to confirm RNA-seq analysis. Data are expressed as mean ± SD; n = 3. PP, Protein Processing. **p < 0.01, ***p < 0.001, ****p < 0.0001 (unpaired t test)

To assess inhibitory effects of azathioprine under conditions resembling typical culture conditions, we generated uniform 3D spheroids using ultra-low attachment 96-well plates and treated them with azathioprine at various concentrations. Azathioprine also induced cell death in 3D spheroids culture conditions (Figure 2C; IC50: 2.4 μM in 559T, 2.2 μM in 592T). Importantly, we did not observe cytotoxicity against normal human astrocytes (NHA) treated with effective azathioprine concentrations (Figure 2D).

Genome-wide analysis indicates that azathioprine modulates pathways regulating GBM survival

To gain insight into anti-cancer effects of azathioprine treatment, we evaluated transcriptional outcomes using mRNA-sequencing (mRNA-seq) in 559T and 592T cells treated with azathioprine. This comparison identified a total 665 differentially expressed genes (DEGs) in 559T and 1,427 DEGs in 592T cells (Figure 3A). To identify pathways altered by azathioprine treatment, we then performed KEGG pathway analysis using up- or downregulated gene clusters. Genes functioning in apoptosis, ferroptosis, protein processing in the ER, and metabolic pathways were upregulated by azathioprine (Figures 3B and 3C). We then validated RNA-seq results by individual qPCR (Figures 3B and 3C). Numerous genes associated with ER stress were upregulated by azathioprine treatment, including C/EBP homologous protein (CHOP), a pro-apoptotic transcription factor (Obacz et al., 2017). Increased CHOP expression is seen in GBM exposed to TMZ (Obacz et al., 2017), and, together with ATF4, CHOP reportedly transcriptionally upregulates the apoptotic genes LC3 and GADD45 (B'chir et al., 2013). Accordingly, CHOP, ATF4, and XBP1, which regulate ER-stress-induced apoptosis, were dramatically induced by azathioprine treatment (Figures 3B and 3C), suggesting that ER-stress-mediated apoptosis may underlie azathioprine effects. Metabolic genes upregulated by azathioprine were associated with oxidation-reduction (such as ALDH3A1, NQO1, and AOC2), suggesting that azathioprine induces oxidative stress in GBM cells. On the other hand, azathioprine treatment downregulated metabolic genes functioning in lipid/cholesterol biosynthesis (such as ACAT2, LIPG, and MSMO1) (Figures 3D and 3E). Many genes functioning in ECM-receptor interaction and regulated by PI3K-AKT signaling (such as THBS2, ITGA6, and COL4A) were also significantly downregulated by azathioprine (Figures 3D and 3E). Overall, these data suggest that azathioprine induces ER-stress-mediated apoptosis and oxidative stress and inhibits lipid metabolism through partial inhibition of PI3K-AKT signaling in GBM.

Global quantitative proteomic profiling identifies proteins associated with cholesterol metabolism as significantly downregulated by azathioprine treatment

To identify pathways most significantly controlled by azathioprine, we profiled global changes in protein expression levels. Such quantitative proteomic analysis was carried out using isobaric tags for relative and absolute quantitation (iTRAQ) coupled with two-dimensional nanoflow liquid chromatography-tandem mass spectrometry (2D-nLC-MS/MS). Azathioprine- or vehicle-treated cells were labeled with isobaric tags, and equal amounts of samples were pooled and analyzed by online 2D-nLC-MS/MS. Two biological replicates were performed, each with two technical replicates. Only proteins quantified at least three times in four replicates were considered in the analysis. We quantified a total of 4,931 proteins in 559T and 4,196 proteins in 592T (Table S2), and azathioprine-treated were compared with vehicle-treated samples to identify differentially expressed proteins. Statistically significant differences in protein abundance were determined based on fold-change with a cut-off of 1.5 and a t test p value threshold of 0.05. Contrary to our predictions, only a few proteins were identified as differentially expressed following azathioprine treatment: 10 downregulated and 3 upregulated in 559T cells and 20 downregulated and 2 upregulated in 592T (Figure 4A and Table S2). Gene ontology (GO) enrichment analysis revealed that downregulated proteins were significantly associated with cholesterol biosynthesis/metabolic processes (Figures 4B and Table S2), whereas we observed no significant enrichment of biological processes following analysis of upregulated proteins. To identify key regulatory pathways controlled by azathioprine, we analyzed proteins commonly regulated in both 559T and 592T cells. Reactome pathway analysis revealed that commonly downregulated proteins (such as LDLR, FDFT1, EPHA2, MSMO1, HMGCS1, and FADS2) were associated

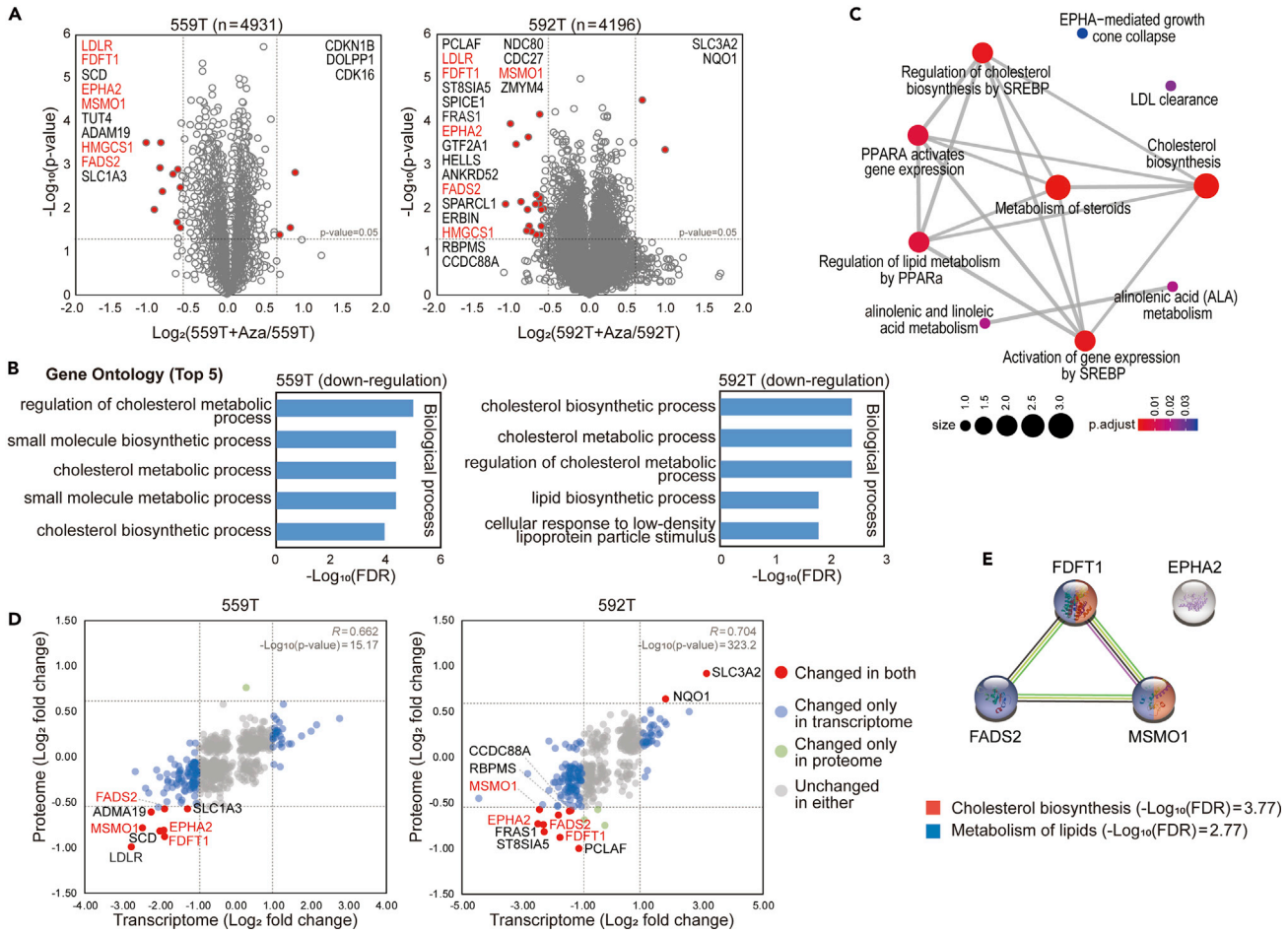

Figure 4. Quantitative profiling of the azathioprine-induced proteome in human glioblastoma 559T and 592T cells

(A–C) 559T or 592T cells were treated with 10 μM azathioprine or DMSO vehicle for 48 h for proteomic analysis. (A) Volcano plots displaying $\log_2$ fold change (azathioprine treatment/control groups) against the -$\log_{10}$ (p value) in 559T (left) and 592T (right) cells. Gray dashed lines indicate the significance threshold (fold-change = 1.5, p value = 0.05). Differentially expressed proteins are highlighted (red dots) with gene names. Six proteins (LDLR, FDFT1, EPHA2, MSMO1, HMGCS1, and FADS2) commonly downregulated in both 559T and 592T cells after azathioprine treatment are marked in red. (B) The top five enriched Gene Ontology terms for biological processes for downregulated proteins in 559T (left) and 592T (right) cells after azathioprine treatment. FDR, false discovery rate. (C) Reactome pathway enrichment map for proteins commonly downregulated in both 559T and 592T cells after azathioprine treatment. Node color indicates pathway significance, and node size indicates the number of genes in the pathway.

(D) Integration of transcriptomic and proteomic data. Scatterplots display expression ratios of proteins and corresponding transcripts in 559T (left) and 592T (right) cells. Gray dashed lines indicate a fold-change cut-off of 2 for transcripts (vertical lines) and a fold-change cut-off of 1.5 for proteins (horizontal lines). Red dots represent expression changes at both protein and transcript levels. Blue and green dots indicate changes in expression only at protein and transcript levels, respectively. Four genes/proteins commonly downregulated in both 559T and 592T cells after azathioprine treatment are marked in red.

(E) Protein-protein interaction (PPI) network of differentially expressed proteins in both the transcriptome and proteome, as determined using the STRING database. Node color indicates enrichment of reactome pathway of proteins. Edges represent meaningful protein-protein associations (green, gene neighborhood; pink, experimentally determined; black, co-expression; yellow, text mining). FDR, false discovery rate.

See also Table S2

with cholesterol biosynthesis and steroid metabolism (Figure 4C). To assess a correlation between changes in RNA and protein expression following azathioprine treatment, we performed integrative analysis. We observed a strong correlation between RNA-seq ($p < 0.05$) and proteomic ($p < 0.05$) data in both 559T ($R = 0.662$) and 592T ($R = 0.704$) cells (Figure 4D). We next evaluated major pathways differentially expressed in the transcriptome and proteome of 559T and 592T cells (such as MSMO1, FDFT1, FADS2, and EPHA2) by constructing a protein-protein interaction (PPI) network using STRING (Search Tool for the Retrieval of Interacting Genes/Proteins) analysis (Figure 4E). Three proteins (MSMO1, FDFT1, and FADS2) were connected with each other in a single module, and they function in cholesterol biosynthesis

and lipid metabolism. Overall, global comprehensive transcriptomic and proteomic analysis rendered a high confidence list of molecules and core pathways regulated by azathioprine.

Azathioprine inhibits EGFR-AKT signaling associated with abnormal lipid metabolism in GBM

As shown in Figure 1, somatic mutations with high or moderate impact on GBM are significantly enriched in metabolic pathways. Altered glucose and lipid metabolism is one of the common features of cancers, including GBM (Zhang and Du, 2012), and several studies report that GBM promotes continuous lipid synthesis and uptake through rewired lipid metabolism (Guo et al., 2011; Oishi et al., 2017; Villa et al., 2016; Zou et al., 2019). To confirm that azathioprine downregulates lipid/cholesterol metabolism in GBM, we first conducted western blot analysis to assess expression of proteins differentially expressed following azathioprine treatment. Decreased LDLR, MSMO1, FDFT1, and FADS2 protein expression was observed in azathioprine-treated cells (Figure 5A). Because lipid/cholesterol synthesis is predominantly controlled by the transcription factor SREBP-1 (Shimano and Sato, 2017), we next assessed the degree of SREBP-1 activation following azathioprine treatment. Interestingly, expression of the mature form of SREBP-1 protein, which activates transcription following nuclear translocation (Wang et al., 1994), was attenuated by azathioprine treatment (Figure 5B). GBM cells also rely on exogenous cholesterol for survival (Villa et al., 2016). LDLR, which mediates cholesterol uptake, is an SREBP-1 target (Guo et al., 2011), and it was also downregulated at both the mRNA and protein levels by azathioprine treatment (Figures 5A and 5C), suggesting that azathioprine blocks cholesterol intake and synthesis in GBM. Next, we asked whether upstream signal of AKT-SREBP1 was regulated by azathioprine. Indeed, EGFR mRNA and protein expression levels were significantly downregulated by azathioprine (Figures 5C–5E), as were downstream targets of EGFR-AKT such as FOXO1A, STAT3, and EPHA2 (Figures 5D and 5E). Azathioprine did not alter kinase activity of EGFR (Figure S1).

To identify if azathioprine affects other GBM cells, we used U87MG and T98G GBM cells, the most used cell lines to study GBM. First, we assessed the viability of these cell lines upon azathioprine treatment. Cell death was induced, but the IC50 values were markedly higher than those of 559T and 592T cells (Figure S2A). In U87MG cells, EGFR, FDFT, and phosphorylated AKT expression was downregulated, whereas in T98G cells, this was not observed even though cell death was induced (Figure S2B). Many studies report that culturing GBM cells in FBS-enriched media induces neural and cancer stem cell differentiation and does not reflect the conditions for brain cell growth *in vivo* because many serum proteins cannot cross the blood-brain barrier (BBB) (Ledur et al., 2017). Therefore, culturing in serum-free and EGF/FGF-based medium and growing in 3D suspension is considered to better mimic the *in vivo* conditions. We reasoned that if U87MG and T98G cells were grown in serum-free 3D culture conditions, such as 559T and 592T cell culture conditions, the response to azathioprine could be altered. Interestingly, U87MG cells grown in serum-free 3D culture conditions showed a higher sensitivity to azathioprine than those grown in FBS-enriched media (IC50: 11.98 μM), whereas azathioprine rarely induced apoptosis in T98G cells grown in serum-free 3D culture conditions (Figure S2C). Western blot analysis also showed that U87MG cells were sensitive to azathioprine treatment (Figure S2D). Because EGFR-targeted therapy has been applied to lung cancer, we examined the effects of azathioprine on lung cancer cells. HCC-95 cells showed sensitivity to azathioprine, whereas A549 cells did not (Figures S2E–S2G).

To determine whether GBM cell death induced by azathioprine occurs as cholesterol is depleted, we analyzed ER-stress-associated apoptotic signaling potentially upregulated by azathioprine. Autophagy is induced to restore homeostasis in early stages of ER stress, but excessive ER stress eventually leads to cell death (Hetz, 2012; Walter and Ron, 2011). We observed both autophagy and apoptosis induced by ER stress following azathioprine treatment based on analysis of autophagy markers, LC3 conversion and p62/SQSTM1, and apoptotic markers, cleaved PARP and cleaved caspase 3 (Figure 5F). We then used transmission electron microscopy (TEM) to assess the ultrastructure of azathioprine-treated cells. Over a 48-h time period, we observed a gradual increase in swelling of the ER (red arrows) and autophagosomes (blue arrows, large double membrane-bound vesicles enclosing cytoplasmic components) in azathioprine-incubated 559T cells (Figure 5G). 592T cells exhibited a gradual increase in autophagosomes over a 48-h time period, whereas swelling of the ER was not observed (Figure 5G). Such observed slight differences in TEM structures between these cell types could be due to differences in genetic background and/or in azathioprine responsiveness. We reasoned that if azathioprine induces GBM cell death by inhibiting the EGFR signaling cascade, reconstitution of EGFR should prevent azathioprine-induced cell death. Consistent with this hypothesis, the introduction of EGFR rescued azathioprine-induced cell death (Figure 5H).

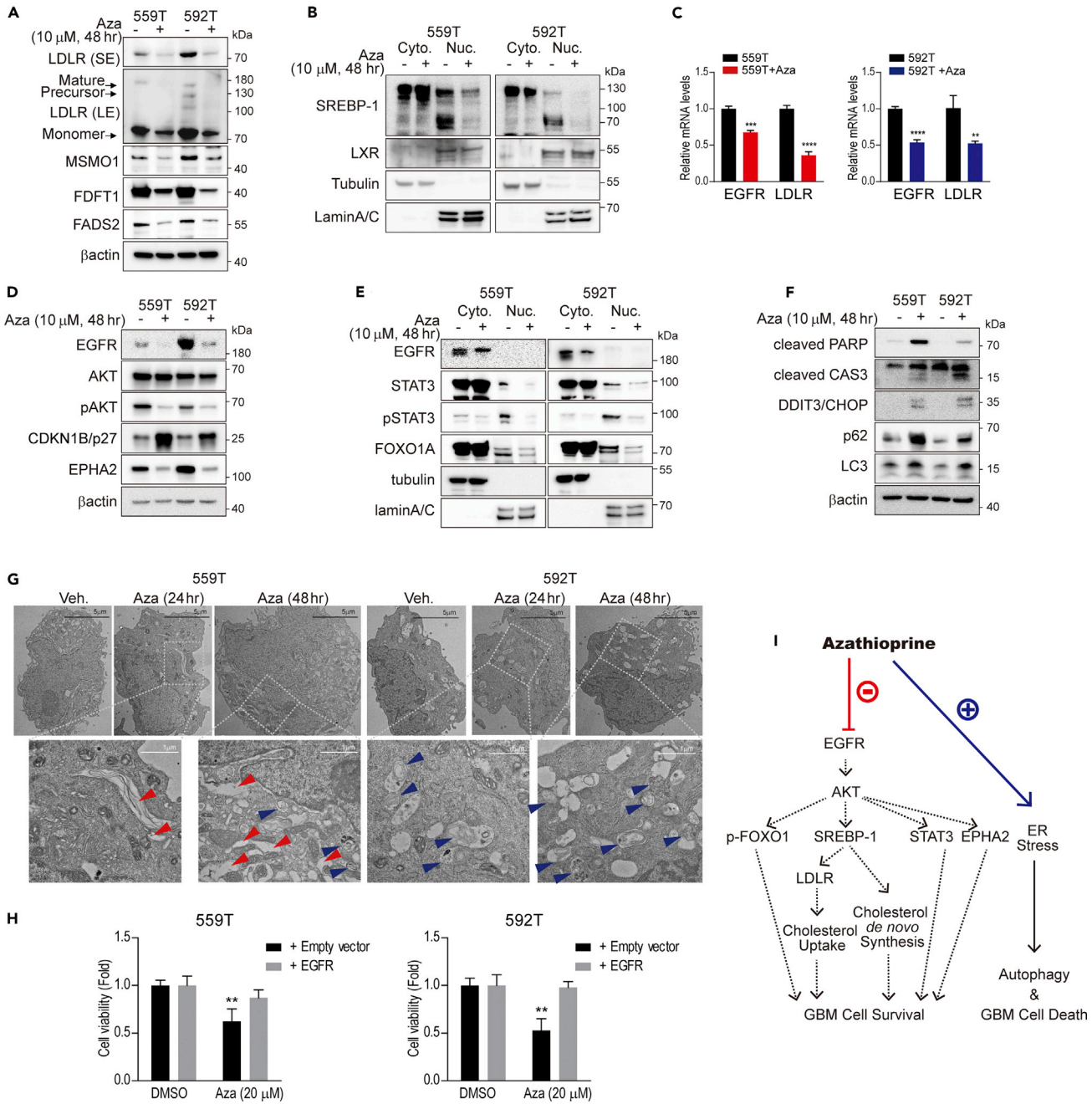

Figure 5. Induction of GBM cell death by azathioprine is accompanied by changes in lipid metabolism

(A, D, and F) Immunoblot analysis of 559T and 592T with indicated antibodies after 48 h of 10 μM azathioprine treatment. β-actin served as loading control.

(B and E) Analysis of subcellular fractions of 559T and 592T following azathioprine treatment, as assessed by immunoblotting. Tubulin served as loading control for cytoplasmic proteins; lamin A/C served as loading control for nuclear proteins.

(C) 559T and 592T cells treated as above were subjected to quantitative RT-PCR analysis. Data are expressed as mean ± SD; n = 3. $^{**}p < 0.01$, $^{***}p < 0.001$, $^{****}p < 0.0001$ (unpaired t test).

(G) Representative TEM image of 559T and 592T cells treated with 10 μM azathioprine for indicated times. Bottom row shows high magnification images. Red arrows represent ER swelling, and blue arrows represent autophagosomes. Black scale bars (upper), 5 μm. White scale bars (down), 1 μm.

(H) Cell viability assay using a CCK-8 kit in 559T or 592T cells. Azathioprine was administered for 48 h. DMSO served as a vehicle. Data are expressed as the mean ± SD; n = 3; $^{**}p < 0.01$ (t test).

(I) Schematic model of signaling cascades regulated by azathioprine.

See also Figures S1 and S2.

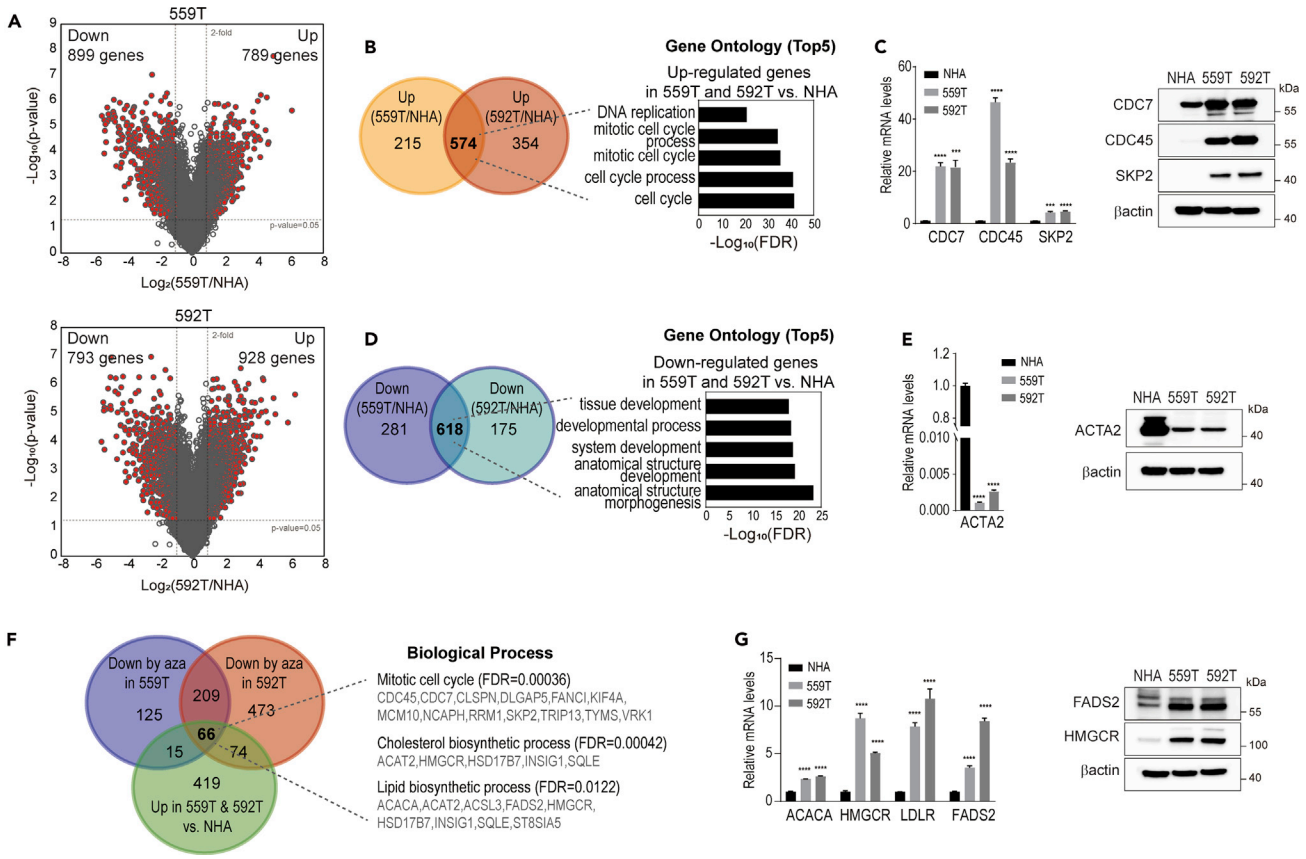

Figure 6. Azathioprine antagonizes genes expression aberrantly expressed in GBM

(A) Volcano plots displaying the $\log_2$ fold-change (GBM/normal human astrocytes (NHA)) against the $-\log_{10}$ (p value) in 559T (up) and 592T (down) cells. Gray dashed lines indicate the significance threshold (fold-change = 2, p value = 0.05). Differentially expressed genes are highlighted (red dots).

(B and D) Venn diagram of gene pools up- (B) or down regulated (D) in indicated GBM lines versus NHA cells. Indicated are the top five enriched Gene Ontology terms for biological processes for up- or downregulated genes in respective groups. FDR, false discovery rate.

(C, E, and G) Quantitative RT-PCR and immunoblot analyses of GBM or NHA cells. Data are expressed as mean ± SD; n = 3. ***p < 0.0001, ****p < 0.0001 (unpaired t test versus NHA). β-actin served as loading control.

(F) Venn diagram of pools downregulated genes in respective groups after azathioprine treatment (top two groups) and pools upregulated genes in 559T and 592T cells versus NHA (below group). Shown are Enriched Gene Ontology terms for biological processes and associated genes. FDR, false discovery rate.

See also Figure S3.

These data indicate that azathioprine inhibits the EGFR signaling cascade associated with lipid metabolism and triggers ER stress to induce GBM cell death (Figure 5I).

Azathioprine antagonizes expression of genes aberrantly expressed in GBM relative to normal astrocytes

We next asked whether azathioprine treatment antagonizes gene expression unique to GBM relative to normal astrocytes (NHA). To do so, we first performed mRNA expression microarray analysis using NHA, 559T, and 592T cells. Compared with NHA cells, 889 genes were downregulated and 789 upregulated in 559T (Figure 6A). In 592T cells, 793 genes were downregulated and 928 genes upregulated relative to NHA cells (Figure 6A). Commonly upregulated genes (574) in 559T and 592T were significantly enriched in cell-cycle-associated processes (Figure 6B). Individual qPCR and western blot analyses confirmed that cell-cycle-associated genes (such as CDC7, CDC45, and SKP2) were overexpressed in 559T and 592T relative to NHA cells (Figure 6C). When we analyzed commonly downregulated genes (618), those gene pools were significantly enriched in anatomical-structure-associated processes (Figure 6D), as exemplified by α smooth muscle actin encoded by ACTA2 (Figure 6E). We then compared gene pools downregulated by azathioprine in 559T and 592T and upregulated in 559T and 592T versus NHA. Interestingly, azathioprine

specifically reduced expression of lipid-/cholesterol-biosynthesis-associated genes as well as those associated with the cell cycle (Figures 6F and S3A). Individual qPCR analysis confirmed upregulation of cholesterol-/lipid-metabolism-associated genes (such as ACACA, HMGCR, INSIG1, LDLR, and FADS2) in 559T and 592T relative to NHA cells (Figure 6G). Gene pools upregulated by azathioprine in 559T and 592T and downregulated in 559T and 592T versus NHA were not significantly enriched in specific biological processes (Figure S3B). Overall, we conclude that azathioprine specifically inhibits cholesterol-/lipid-biosynthesis-related and cell-cycle-associated genes among the hundreds of genes differently expressed in GBM compared with NHA.

In vivo efficacy of azathioprine in a GBM model

Before testing the *in vivo* efficacy of azathioprine, we needed to determine the sensitivity of standard therapy for GBM in an *in vivo* system. 559T cells were used to generate orthotopic xenograft models, which were treated with TMZ or exposed to radiation commonly applied in combination with chemotherapy. There was no significant increase in lifespan among vehicle-, TMZ-, or radiation-treated groups (Figure 7A). However, combinatorial treatment with azathioprine significantly increased the lifespan (Figure 7B).

To monitor tumor growth in real time, we established patient-derived primary 592T-luciferase GBM cells by stably expressing luciferase in this line to allow *in vivo* luminescence imaging. We then intracranially (i.c.) injected cells into immune-compromised mice to evaluate tumor progression. After 2 weeks, we selected mice with similar body weights and tumor size and began daily treatment with azathioprine or TMZ alone or with combined azathioprine + TMZ during which time we analyzed tumor size by luciferase imaging every 4 days (Figure 7C). According to standard TMZ therapy regimen (Brada et al., 2001), TMZ was administered once daily for the first 5 days during the entire treatment period. We observed no significant changes in body weight between groups (Figure 7D). Vehicle-treated mice exhibited rapid tumorigenesis within 5 weeks of injection. Combined azathioprine + TMZ treatment dramatically reduced tumor size (Figures 7C and 7E). TMZ or azathioprine treatment alone slightly inhibited tumor size at the initial time point, but none of the GBM tumors in either treatment group showed significant tumor reduction at the endpoint (Figures 7C and 7E). We then performed immunohistochemistry (IHC) of brain tumors from sacrificed mice in all groups (Figure 7F). Levels of apoptotic marker proteins such as cleaved caspase 3 and cleaved PARP increased in the azathioprine-alone and the TMZ co-treated group compared with vehicle-treated group (Figures 7G and 7H). The TMZ-alone treated group showed an increase in cleaved PARP but no significant increase in cleaved caspase 3. The proliferation marker protein Ki67 also significantly decreased in azathioprine alone, TMZ alone, and TMZ co-treated groups compared with vehicle-treated group (Figure 7I). To confirm that azathioprine inhibits lipid metabolism in GBM *in vivo*, we verified expression levels of representative upregulated lipid-metabolism-associated proteins in GBM. We observed a significant decrease in MSMO1, FADS2, and FDFT1 expression levels in the azathioprine alone and TMZ co-treated groups relative to vehicle-treated group but not in TMZ-treated group (Figures 7J–7L). These data indicate that co-treatment with azathioprine and TMZ induces apoptosis of GBM *in vivo* and simultaneously alters lipid metabolism.

DISCUSSION

In this study, we identify azathioprine as a promising drug that could be repurposed for GBM treatment, based on a high-throughput screen to identify drugs effective against two subtypes of TMZ-resistant GBM. Genome-wide analysis and global proteomic analysis revealed that azathioprine treatment lowers abnormally upregulated cholesterol/lipid biosynthesis and uptake and induces ER stress and apoptosis. We also show that azathioprine significantly alters oncogenic phenotypes of GBM, such as perturbations in the cell cycle. An *in vivo* test of efficacy using a GBM orthotropic xenograft mouse model confirmed the effect of azathioprine in inducing GBM cell death and also revealed inhibition of aberrant lipid metabolism by drug treatment. In addition, combination treatment with TMZ showed a dramatic reduction in tumor volumes in xenograft model. Our study suggests that a drug repurposing (or repositioning) strategy for azathioprine could provide a viable pharmacological therapy for GBM patients.

Drug repurposing strategies have many advantages, including lower risk and more rapid development, and are associated with lower-than-average associated costs (Pushpakom et al., 2019). Moreover, because azathioprine has already been approved as an immunosuppressive medication, it is less likely to fail a safety trial. Nonetheless, further analysis is required to determine its clinical efficacy for the treatment of GBM patients.

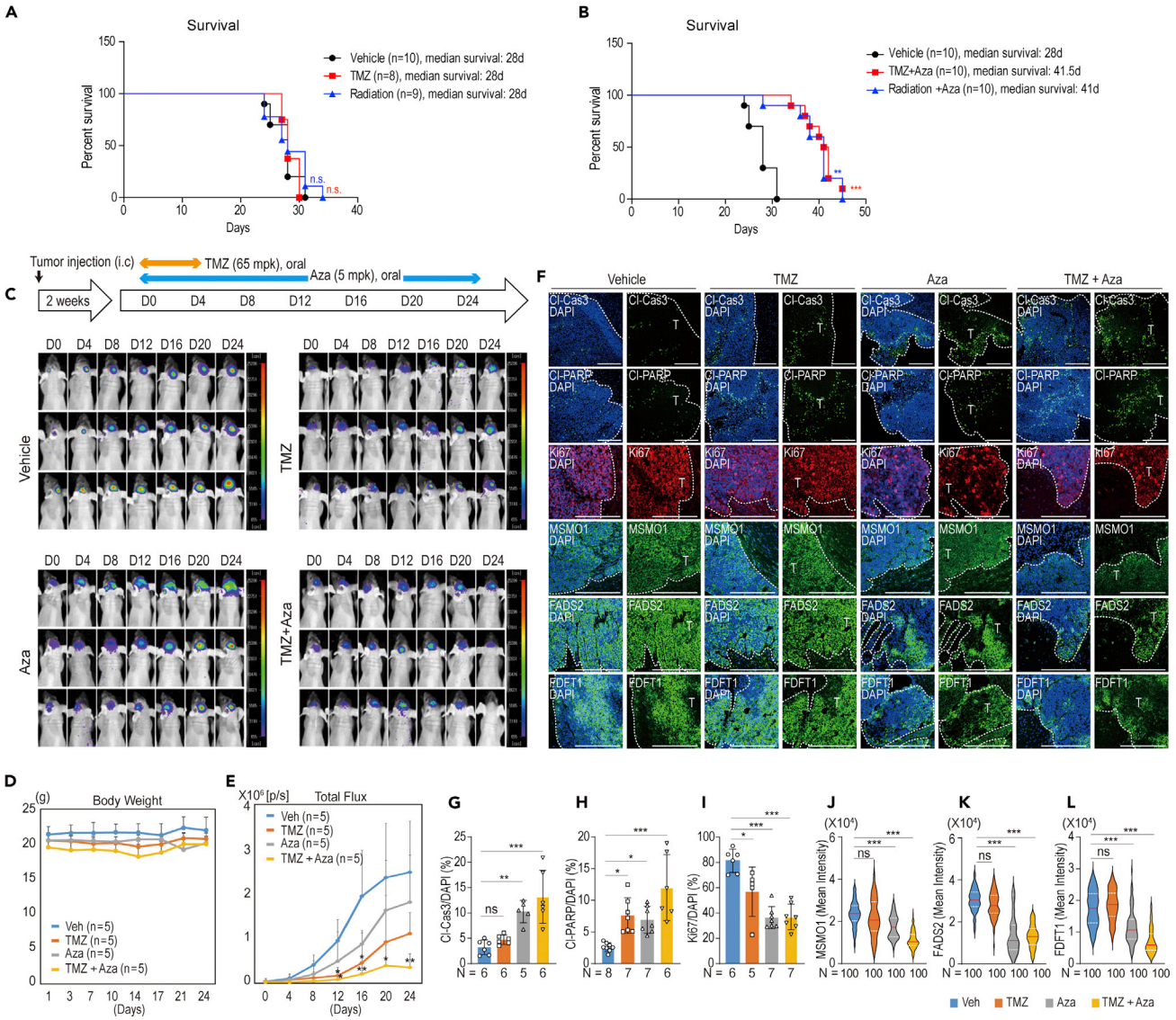

Figure 7. *In vivo* xenograft model reveals that azathioprine induces GBM cell apoptosis accompanied by changes in lipid metabolism

(A and B) Survival rate of the xenograft model. Temozolomide (TMZ, 65 mg/kg) was administered orally for 5 days daily beginning the 17th day after GBM cell implantation. Xenograft models were exposed to 2 Gy of radiation for 5 days daily beginning the 17th day after GBM cell implantation. Azathioprine (Aza, 20 mg/kg) was administered daily orally from the 11th day after GBM cell implantation. **p < 0.01, ***p < 0.001 (Log rank (Mantel-Cox) test).

(C) Schematic showing GBM injection and drug treatment schedule. Xenograft models were grouped as TMZ only, Aza only, TZM + Aza combination, and controls (vehicle-treated) once luciferase-expressing tumors were detected (D0), and daily oral administration with indicated drugs was then initiated. Tumors were imaged every 4 days, and animals were sacrificed at D24. Shown are representative images of *in vivo* luciferase activity. N = 5 for each group.

(D) Body weights of each group, as measured every 3–4 days. Data are expressed as mean ± SD; n = 5. There were no significant differences among groups.

(E) Luciferase activity, as measured every 4 days. Quantification (total flux, photons per second = p/s) of bioluminescent signals from tumor regions. Data are expressed as mean ± SD; n = 5. *p < 0.05, **p < 0.01 (one-way ANOVA, Tukey's multiple comparison test).

(F) Representative confocal images of IHC samples from orthotopic GBM xenograft tumors probed with indicated antibodies. Tumors (T) are inside the white dotted line. Scale bars, 200 μm.

(G–I) Intensity of IHC staining in indicated groups, as quantified using the ImageJ program. Ratios were determined by dividing antibody intensity by that of DAPI. Data are expressed as mean ± SD; *p < 0.05, **p < 0.01, ***p < 0.001 (one-way ANOVA, Tukey's multiple comparison test).

(J–L) Intensity of IHC staining in 100 cells from indicated groups, as quantified using the ImageJ program. Ratios were determined by dividing the intensity of indicated antibodies by that of DAPI. Data are expressed as mean ± SD; ***p < 0.001 (one-way ANOVA, Tukey's multiple comparison test).

Elevated lipid metabolism is a characteristic of GBM, and EGFR/AKT/SREBP-1 signaling regulates GMB growth and survival by activating lipid metabolism. Our analysis reveals the unanticipated finding that azathioprine likely controls cholesterol/lipid biosynthesis and uptake by blocking EGFR/AKT/SREBP-1 signaling. Relevant to other approaches, the transcription factor liver X receptor (LXR) reportedly decreased excess cholesterol levels by promoting efflux through sterol transporters such as ABCA1 (Guo et al., 2011). Because reagents that activate LXR have been studied as new GBM therapies based on induction of cholesterol efflux (Guo et al., 2011; Villa et al., 2016), we asked whether azathioprine regulates LXR. LXR protein levels and ABCA1 mRNA levels were not significantly altered by azathioprine treatment, suggesting that azathioprine does not alter cholesterol efflux (Figure 5B and mRNA-seq data).

Both the rate-limiting enzyme in cholesterol synthesis, 3-hydroxy-3-methyl-glutaryl-coenzyme A (HMG-CoA) reductase (HMGCR), as well as LDLR are critical for uptake of extracellular cholesterol (Brown et al., 2018). We found that HMGCR and LDLR were significantly overexpressed in GBM relative to NHA. Normally, HMGCR and LDLR expression are suppressed by cholesterol accumulation (Luo et al., 2020), a negative feedback loop controlled by SREBP transcription factors (Brown and Goldstein, 1997). Following sterol depletion, SREBPs are released from the ER membrane through proteolytic cleavage and translocated to the nucleus (Brown and Goldstein, 1997). Contrary to the regulatory mechanism of SREBPs in normal cells, we found that SREBP-1 in 559T or 592T cells resides in the nucleus regardless of the presence of sterol. It is thought that abnormal nuclear accumulation of SREBP-1 in GBM disrupts the feedback loop controlling lipid biosynthesis and contributes to GBM growth and survival. Therefore, targeting SREBP-1 and the lipogenic machinery could be a promising anti-cancer strategy. Indeed, treatment with HMGCR inhibitors such as statins or SREBP inhibitors such as fatostatin or betulin show promising results in inhibiting tumor growth (Gholkar et al., 2016; Li et al., 2015).

We found that EGFR, whose signaling underlies aberrant lipid metabolism, is downregulated by azathioprine. We were surprised by the results because azathioprine has no known function related to EGFR inhibition. Our current findings raise the possibility of azathioprine as a promising drug not only for GBM treatment but also for lung or colorectal cancer patients with amplified EGFR. Interestingly, as azathioprine modulates EGFR transcriptionally, EGFR mutant genes would also be downregulated by azathioprine. We detected the somatic mutation (R521K) in EGFR in both 559T and 592T cells, although that mutation has been considered polymorphic rather than functionally significant, as it does not alter the charge of the relevant amino acid and is detected in numerous patients with colorectal, lung, and brain tumors (Lassman et al., 2005). 592T cells have amplified EGFR expressions compared with 559T cells (Figure 5D), but inhibitory azathioprine concentrations were comparable in both cell types (Figures 2B and 2C). In addition, aberrant upregulation of lipid metabolism, which is controlled by EGFR activation, was comparable in 559T and 592T cells despite different EGFR expression status. These data indicate that unknown upstream components may also govern rewired lipid metabolism seen in GBM and warrant future analysis.

Finally, our results show that azathioprine induces GBM cell apoptosis. TMZ reportedly induces ER stress in GBM cells (Obacz et al., 2017), and numerous studies propose that perturbation of ER homeostasis is a promising strategy to induce cancer cell death (Obacz et al., 2017; Penaranda Fajardo et al., 2016). Interestingly, azathioprine also promotes excessive ER stress, and cladribine and fludarabine, which are also purine analogs, reportedly induce ER stress and the UPR (Mactier et al., 2011). Thus induction of ER stress could be a general outcome of treatment with purine analogs. Overall, our study provides strong evidence that azathioprine antagonizes GBM progression and deserves further consideration as a potential therapeutic strategy for GBM patients.

Limitations of the study

In this study, we primarily investigated the therapeutic effects of azathioprine on GBM. Through integrative RNA-sequencing and proteomic analysis, we found that this compound markedly inhibits the cholesterol biosynthesis pathway, triggers ER stress response, induces autophagy, and promotes apoptosis. Although these effects of azathioprine were confirmed through several biochemical experiments and *in vivo* studies, the molecules that azathioprine directly targets in GBM remain unknown. In addition, the mechanism through which azathioprine downregulates EGFR expression has not been completely elucidated. Although the mechanistic insights into the action of azathioprine in GBM are slightly lacking in the multiple pathways described in the study, we validated the possibility of azathioprine in treating GBM through the

current study. However, the certification of azathioprine metabolism in GBM, comparison of the effects of other anti-metabolite compounds related to azathioprine on GBM cells, and *in vitro* experiments on dual treatment with TMZ and azathioprine need to be conducted in future studies. Finally, the ability of azathioprine to cross the BBB in GBM in clinical settings should be studied prior to its application as a therapeutic drug for GBM patients.

Resource availability

Lead contact

Further information and requests for resources and reagents should be directed to and will be fulfilled by the lead contact Heeyeong Cho (hycho@krict.re.kr).

Materials availability

This study did not generate new unique reagents.

Data and code availability

The accession number for the RNA-seq, WES, microarray data reported in this paper is GEO: GSE153908. Original data have been deposited to Mendeley Data: https://data.mendeley.com/datasets/96mmjs2jkr/draft?a=022a0a44-fa8a-4c1c-95cf-9b5c244ed558.

METHODS

All methods can be found in the accompanying transparent methods supplemental file.

SUPPLEMENTAL INFORMATION

Supplemental information can be found online at https://doi.org/10.1016/j.isci.2021.102238.

ACKNOWLEDGMENTS

This work was supported by a grant from the Korea Research Institute of Chemical Technology (Project number SI-2031-50); the Bio & Medical Technology Development Program of the National Research Foundation (NRF) was funded by the Ministry of Science & ICT (2020M3A9I4036072).

AUTHOR CONTRIBUTIONS

H.J.N. and H.C. designed experiments and gathered and analyzed overall results; H.J.N. performed cell biology and biochemistry experiments and sample preparation for WES, RNA-seq, and proteomics; S.C. and J.W.J. performed cell biology and biochemistry experiments; Y.E.K. performed LC-MS/MS and proteomic analysis; B.-S. M. and D.-H.N. conducted the *in vivo* assay; H.Y.K. and D. J. performed HTS; D.-H.N. provided patient-derived GBM cells; H.J.N., Y.E.K, B.-S. M., and H.C. wrote the manuscript.

DECLARATION OF INTERESTS

The authors declare no competing interests.

Received: October 12, 2020
Revised: January 29, 2021
Accepted: February 23, 2021
Published: March 19, 2021

REFERENCES

Alphandéry, E. (2018). Glioblastoma treatments: an account of recent industrial developments. Front. Pharmacol. *9*, 879.

B'chir, W., Maurin, A.-C., Carraro, V., Averous, J., Jousse, C., Muranishi, Y., Parry, L., Stepien, G., Fafournoux, P., and Bruhat, A. (2013). The eIF2α/ATF4 pathway is essential for stress-induced autophagy gene expression. Nucleic Acids Res. *41*, 7683–7699.

Baker, S.D., Wirth, M., Statkevich, P., Reidenberg, P., Alton, K., Sartorius, S.E., Dugan, M., Cutler, D., Batra, V., Grochow, L.B., et al. (1999). Absorption, metabolism, and excretion of 14C-temozolomide following oral administration to patients with advanced cancer. Clin. Cancer Res. *5*, 309–317.

Brada, M., Hoang-Xuan, K., Rampling, R., Dietrich, P.-Y., Dirix, L., Macdonald, D., Heimans, J., Zonnenberg, B., Bravo-Marques, J., and Henriksson, R. (2001). Multicenter phase II trial of temozolomide in patients with glioblastoma multiforme at first relapse. Ann. Oncol. *12*, 259–266.

Brennan, C.W., Verhaak, R.G., McKenna, A., Campos, B., Noushmehr, H., Salama, S.R., Zheng, S., Chakravarty, D., Sanborn, J.Z., Berman, S.H., et al. (2013). The somatic genomic landscape of

glioblastoma. Cell *155*, 462–477, https://doi.org/10.1016/j.cell.2013.09.034.

Brown, M.S., and Goldstein, J.L. (1997). The SREBP pathway: regulation of cholesterol metabolism by proteolysis of a membrane-bound transcription factor. Cell *89*, 331–340, https://doi.org/10.1016/s0092-8674(00)80213-5.

Brown, M.S., Radhakrishnan, A., and Goldstein, J.L. (2018). Retrospective on cholesterol homeostasis: the central role of scap. Annu. Rev. Biochem. *87*, 783–807, https://doi.org/10.1146/annurev-biochem-062917-011852.

Cantor, J.R., and Sabatini, D.M. (2012). Cancer cell metabolism: one hallmark, many faces. Cancer Discov. *2*, 881–898, https://doi.org/10.1158/2159-8290.CD-12-0345.

Cheng, C., Geng, F., Cheng, X., and Guo, D. (2018a). Lipid metabolism reprogramming and its potential targets in cancer. Cancer Commun. *38*, 27, https://doi.org/10.1186/s40880-018-0301-4.

Cheng, X., Li, J., and Guo, D. (2018b). SCAP/SREBPs are central players in lipid metabolism and novel metabolic targets in cancer therapy. Curr. Top. Med. Chem. *18*, 484–493, https://doi.org/10.2174/1568026618666180523104541.

Germano, G., Amirouchene-Angelozzi, N., Rospo, G., and Bardelli, A. (2018). The clinical impact of the genomic landscape of mismatch repair-deficient cancers. Cancer Discov. *8*, 1518–1528, https://doi.org/10.1158/2159-8290.CD-18-0150.

Gholkar, A.A., Cheung, K., Williams, K.J., Lo, Y.C., Hamideh, S.A., Nnebe, C., Khuu, C., Bensinger, S.J., and Torres, J.Z. (2016). Fatostatin inhibits cancer cell proliferation by affecting mitotic microtubule spindle assembly and cell division. J. Biol. Chem. *291*, 17001–17008, https://doi.org/10.1074/jbc.C116.737346.

Gimple, R.C., Kidwell, R.L., Kim, L.J.Y., Sun, T., Gromovsky, A.D., Wu, Q., Wolf, M., Lv, D., Bhargava, S., Jiang, L., et al. (2019). Glioma stem cell-specific superenhancer promotes polyunsaturated fatty-acid synthesis to support EGFR signaling. Cancer Discov. *9*, 1248–1267, https://doi.org/10.1158/2159-8290.CD-19-0061.

Guo, D., Bell, E.H., Mischel, P., and Chakravarti, A. (2014). Targeting SREBP-1-driven lipid metabolism to treat cancer. Curr. Pharm. Des. *20*, 2619–2626, https://doi.org/10.2174/13816128113199990486.

Guo, D., Prins, R.M., Dang, J., Kuga, D., Iwanami, A., Soto, H., Lin, K.Y., Huang, T.T., Akhavan, D., and Hock, M.B. (2009). EGFR signaling through an Akt-SREBP-1–dependent, rapamycin-resistant pathway sensitizes glioblastomas to antilipogenic therapy. Sci. Signal. *2*, ra82, https://doi.org/10.1126/scisignal.2000446.

Guo, D., Reinitz, F., Youssef, M., Hong, C., Nathanson, D., Akhavan, D., Kuga, D., Amzajerdi, A.N., Soto, H., Zhu, S., et al. (2011). An LXR agonist promotes glioblastoma cell death through inhibition of an EGFR/AKT/SREBP-1/LDLR-dependent pathway. Cancer Discov. *1*, 442–456, https://doi.org/10.1158/2159-8290.CD-11-0102.

Hanahan, D., and Weinberg, R.A. (2011). Hallmarks of cancer: the next generation. Cell *144*, 646–674, https://doi.org/10.1016/j.cell.2011.02.013.

Harfe, B.D., and Jinks-Robertson, S. (2000). DNA mismatch repair and genetic instability. Annu. Rev. Genet. *34*, 359–399, https://doi.org/10.1146/annurev.genet.34.1.359.

Hetz, C. (2012). The unfolded protein response: controlling cell fate decisions under ER stress and beyond. Nat. Rev. Mol. Cell Biol. *13*, 89–102.

Jiricny, J., and Nystrom-Lahti, M. (2000). Mismatch repair defects in cancer. Curr. Opin. Genet. Dev. *10*, 157–161, https://doi.org/10.1016/s0959-437x(00)00066-6.

Joo, K.M., Kim, J., Jin, J., Kim, M., Seol, H.J., Muradov, J., Yang, H., Choi, Y.L., Park, W.Y., Kong, D.S., et al. (2013). Patient-specific orthotopic glioblastoma xenograft models recapitulate the histopathology and biology of human glioblastomas in situ. Cell Rep. *3*, 260–273, https://doi.org/10.1016/j.celrep.2012.12.013.

Karran, P., and Attard, N. (2008). Thiopurines in current medical practice: molecular mechanisms and contributions to therapy-related cancer. Nat. Rev. Cancer *8*, 24–36, https://doi.org/10.1038/nrc2292.

Kung, C.P., Leu, J.I., Basu, S., Khaku, S., Anokye-Danso, F., Liu, Q., George, D.L., Ahima, R.S., and Murphy, M.E. (2016). The P72R polymorphism of p53 predisposes to obesity and metabolic dysfunction. Cell Rep. *14*, 2413–2425, https://doi.org/10.1016/j.celrep.2016.02.037.

Lassman, A.B., Rossi, M.R., Raizer, J.J., Abrey, L.E., Lieberman, F.S., Grefe, C.N., Lamborn, K., Pao, W., Shih, A.H., Kuhn, J.G., et al. (2005). Molecular study of malignant gliomas treated with epidermal growth factor receptor inhibitors: tissue analysis from North American Brain Tumor Consortium Trials 01-03 and 00-01. Clin. Cancer Res. *11*, 7841–7850, https://doi.org/10.1158/1078-0432.CCR-05-0421.

Ledur, P.F., Onzi, G.R., Zong, H., and Lenz, G. (2017). Culture conditions defining glioblastoma cells behavior: what is the impact for novel discoveries? Oncotarget *8*, 69185.

Li, X., Wu, J.B., Chung, L.W., and Huang, W.C. (2015). Anti-cancer efficacy of SREBP inhibitor, alone or in combination with docetaxel, in prostate cancer harboring p53 mutations. Oncotarget *6*, 41018–41032, https://doi.org/10.18632/oncotarget.5879.

Luo, J., Yang, H., and Song, B.L. (2020). Mechanisms and regulation of cholesterol homeostasis. Nat. Rev. Mol. Cell Biol *21*, 225–245, https://doi.org/10.1038/s41580-019-0190-7.

Mactier, S., Henrich, S., Che, Y., Kohnke, P.L., and Christopherson, R.I. (2011). Comprehensive proteomic analysis of the effects of purine analogs on human Raji B-cell lymphoma. J. Proteome Res. *10*, 1030–1042, https://doi.org/10.1021/pr100803b.

Mansouri, A., Hachem, L.D., Mansouri, S., Nassiri, F., Laperriere, N.J., Xia, D., Lindeman, N.I., Wen, P.Y., Chakravarti, A., Mehta, M.P., et al. (2019). MGMT promoter methylation status testing to guide therapy for glioblastoma: refining the approach based on emerging evidence and current challenges. Neuro Oncol. *21*, 167–178, https://doi.org/10.1093/neuonc/noy132.

Meyer, M., Reimand, J., Lan, X., Head, R., Zhu, X., Kushida, M., Bayani, J., Pressey, J.C., Lionel, A.C., Clarke, I.D., et al. (2015). Single cell-derived clonal analysis of human glioblastoma links functional and genomic heterogeneity. Proc. Natl. Acad. Sci. U S A *112*, 851–856, https://doi.org/10.1073/pnas.1320611111.

Obacz, J., Avril, T., Le Reste, P.J., Urra, H., Quillien, V., Hetz, C., and Chevet, E. (2017). Endoplasmic reticulum proteostasis in glioblastoma-From molecular mechanisms to therapeutic perspectives. Sci. Signaling *10*, eaal2323, https://doi.org/10.1126/scisignal.aal2323.

Oh, Y.T., Cho, H.J., Kim, J., Lee, J.H., Rho, K., Seo, Y.J., Choi, Y.S., Jung, H.J., Song, H.S., Kong, D.S., et al. (2014). Translational validation of personalized treatment strategy based on genetic characteristics of glioblastoma. PLoS One *9*, e103327, https://doi.org/10.1371/journal.pone.0103327.

Oishi, Y., Spann, N.J., Link, V.M., Muse, E.D., Strid, T., Edillor, C., Kolar, M.J., Matsuzaka, T., Hayakawa, S., Tao, J., et al. (2017). SREBP1 contributes to resolution of pro-inflammatory TLR4 signaling by reprogramming fatty acid metabolism. Cell Metab. *25*, 412–427, https://doi.org/10.1016/j.cmet.2016.11.009.

Olivier, M., Hollstein, M., and Hainaut, P. (2010). TP53 mutations in human cancers: origins, consequences, and clinical use. Cold Spring Harb. Perspect. Biol. *2*, a001008, https://doi.org/10.1101/cshperspect.a001008.

Penaranda Fajardo, N.M., Meijer, C., and Kruyt, F.A. (2016). The endoplasmic reticulum stress/unfolded protein response in gliomagenesis, tumor progression and as a therapeutic target in glioblastoma. Biochem. Pharmacol. *118*, 1–8, https://doi.org/10.1016/j.bcp.2016.04.008.

Pushpakom, S., Iorio, F., Eyers, P.A., Escott, K.J., Hopper, S., Wells, A., Doig, A., Guilliams, T., Latimer, J., McNamee, C., et al. (2019). Drug repurposing: progress, challenges and recommendations. Nat. Rev. Drug Discov. *18*, 41–58, https://doi.org/10.1038/nrd.2018.168.

Rahman, M., and Hasan, M.R. (2015). Cancer metabolism and drug resistance. Metabolites *5*, 571–600, https://doi.org/10.3390/metabo5040571.

Shimano, H., and Sato, R. (2017). SREBP-regulated lipid metabolism: convergent physiology - divergent pathophysiology. Nat. Rev. Endocrinol. *13*, 710–730, https://doi.org/10.1038/nrendo.2017.91.

Stupp, R., Hegi, M.E., Gilbert, M.R., and Chakravarti, A. (2007). Chemoradiotherapy in malignant glioma: standard of care and future directions. J. Clin. Oncol. *25*, 4127–4136, https://doi.org/10.1200/JCO.2007.11.8554.

Tamimi, A.F., and Juweid, M. (2017). Epidemiology and outcome of glioblastoma. In Glioblastoma, S. De Vleeschouwer, ed. (Codon Publications), pp. 143–153.

Verhaak, R.G., Hoadley, K.A., Purdom, E., Wang, V., Qi, Y., Wilkerson, M.D., Miller, C.R., Ding, L., Golub, T., Mesirov, J.P., et al. (2010). Integrated genomic analysis identifies clinically relevant subtypes of glioblastoma characterized by abnormalities in PDGFRA, IDH1, EGFR, and NF1. Cancer Cell *17*, 98–110, https://doi.org/10.1016/j.ccr.2009.12.020.

Villa, G.R., Hulce, J.J., Zanca, C., Bi, J., Ikegami, S., Cahill, G.L., Gu, Y., Lum, K.M., Masui, K., Yang, H., et al. (2016). An LXR-cholesterol Axis creates a metabolic Co-dependency for brain cancers. Cancer Cell *30*, 683–693, https://doi.org/10.1016/j.ccell.2016.09.008.

Walter, P., and Ron, D. (2011). The unfolded protein response: from stress pathway to homeostatic regulation. Science *334*, 1081–1086.

Wang, X., Sato, R., Brown, M.S., Hua, X., and Goldstein, J.L. (1994). SREBP-1, a membrane-bound transcription factor released by sterol-regulated proteolysis. Cell *77*, 53–62, https://doi.org/10.1016/0092-8674(94)90234-8.

Wang, X., Yang, K., Xie, Q., Wu, Q., Mack, S.C., Shi, Y., Kim, L.J.Y., Prager, B.C., Flavahan, W.A., Liu, X., et al. (2017). Purine synthesis promotes maintenance of brain tumor initiating cells in glioma. Nat. Neurosci. *20*, 661–673, https://doi.org/10.1038/nn.4537.

Zhang, F., and Du, G. (2012). Dysregulated lipid metabolism in cancer. World J. Biol. Chem. *3*, 167–174, https://doi.org/10.4331/wjbc.v3.i8.167.

Zou, Y., Watters, A., Cheng, N., Perry, C.E., Xu, K., Alicea, G.M., Parris, J.L.D., Baraban, E., Ray, P., Nayak, A., et al. (2019). Polyunsaturated fatty acids from astrocytes activate PPARgamma signaling in cancer cells to promote brain metastasis. Cancer Discov. *9*, 1720–1735, https://doi.org/10.1158/2159-8290.CD-19-0270.

iScience, Volume *24*

Supplemental information

Azathioprine antagonizes aberrantly elevated lipid metabolism and induces apoptosis in glioblastoma

Hye Jin Nam, Young Eun Kim, Byoung-San Moon, Hyun Young Kim, Daeyoung Jung, Seungho Choi, Jeong Woon Jang, Do-Hyun Nam, and Heeyeong Cho

Supplemental Information

Supplemental Data Items:

Supplemental Figures 1, 2, and 3

Transparent Methods

Supplemental References

Supplemental Figure 1

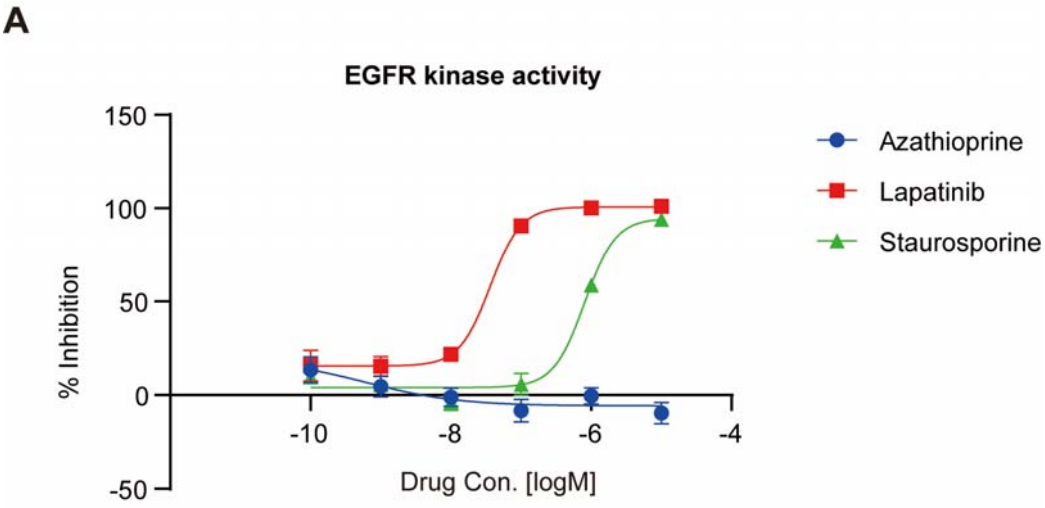

Figure S1, Related to Figure 5. Azathioprine does not inhibit kinase activity of EGFR

(A) EGFR kinase assay using EGFR kinase enzyme system and ADP-Glo kinase assay kit was performed after serially-diluted indicated drugs. Dose-response curve fitting used nonlinear regression. Data are expressed as Mean ± SD; n=3.

Supplemental Figure 2

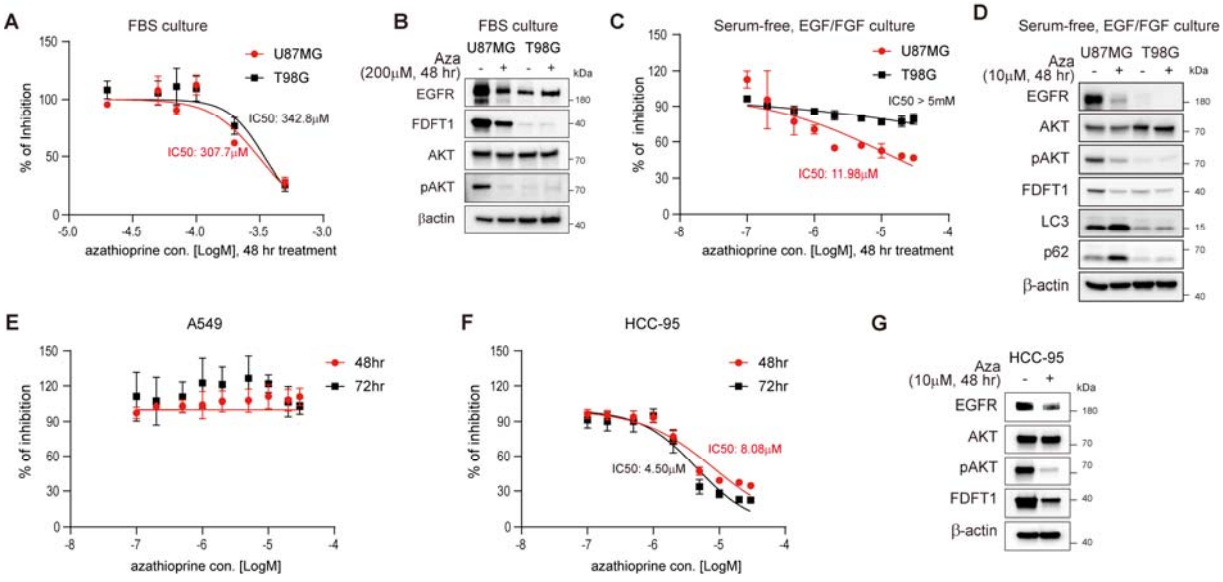

Figure S2, Related to Figure 5. Effects of azathioprine on other GBM cells and lung cancer cells.

(A, C and E-F) 2D viability assay using a CCK-8 kit (A, E, F) or a 3D viability assay using the CellTiter-Glo 3D cell viability kit (C). Both assays were performed after treatment with serially-diluted azathioprine for indicated time. Dose-response curve fitting used nonlinear regression. Data are expressed as Mean ± SD; n = 3-4. DMSO served as vehicle. **(B, D, and G)** Immunoblot analysis of U87MG, T98G, or HCC-95 using indicated antibodies after 48 hours treatment with azathioprine at the indicated concentrations. β-actin served as loading control.

Supplemental Figure 3

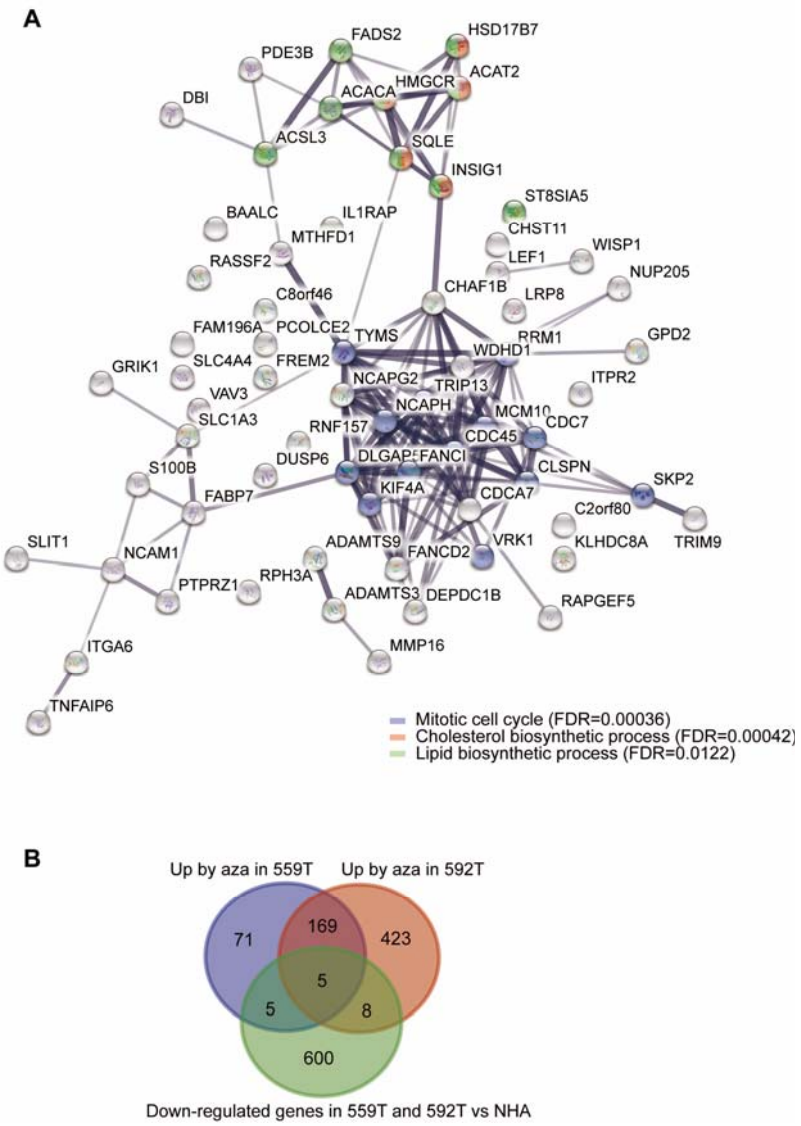

Figure S3, Related to Figure 6. Azathioprine alters some GBM cancer phenotypes

(A) Protein-protein interaction (PPI) network of gene pools down-regulated after azathioprine treatment in 559T and 592T cells and up-regulated in gene pools from 559T and 592T versus NHA cells, based on STRING database. FDR, false discovery rate. **(B)** Venn diagram of pools up-regulated genes in respective groups after azathioprine treatment (top two groups) and pools down-regulated genes in 559T and 592T cells versus NHA (below group).

Transparent Methods

KEY RESOURCES TABLE

REAGENT or RESOURCE	SOURCE	IDENTIFIER
Antibodies		
anti-SREBP-1	Santa Cruze	Cat# sc-13551; RRID:AB_628282
anti-LXR	Santa Cruze	Cat# sc-13068; RRID:AB_2154782
anti-p27	Santa Cruze	Cat# sc-528; RRID:AB_632129
anti-LDLR	abcam	Cat# ab30532
anti-p62	abcam	Cat# ab101266; RRID:AB_10675814
anti-FDFT1	abcam	Cat# ab195046; RRID:AB_2860018
anti-Tubulin	abcam	Cat# ab176560; RRID:AB_2860019
anti-FOXO1A	abcam	Cat# ab52857; RRID:AB_869817
anti-MGMT	Cell Signaling	Cat# 2739; RRID:AB_2297658
anti-EPHA2	Cell Signaling	Cat# 6997; RRID:AB_10827743
anti-EGFR	Cell Signaling	Cat# 2232; RRID:AB_331707
anti-AKT	Cell Signaling	Cat# 4691; RRID:AB_915783
anti-phospho-AKT	Cell Signaling	Cat# 4060; RRID:AB_2315049
anti-STAT3	Cell Signaling	Cat# 9139; RRID:AB_331757
anti-phospho-STAT3	Cell Signaling	Cat# 9145; RRID:AB_2491009
anti-cleaved caspase3	Cell Signaling	Cat# 9661; RRID:AB_2341188
anti-cleaved PARP1	Cell Signaling	Cat# 5625; RRID:AB_10699459
anti-CHOP	Cell Signaling	Cat# 2895; RRID:AB_2089254
anti-LC3	Cell Signaling	Cat# 2775; RRID:AB_915950
anti-CDC7	Cell Signaling	Cat# 3603; RRID:AB_2276095

anti-CDC45	Cell Signaling	Cat# 11881; RRID:AB_2715569
anti-SKP2	Cell Signaling	Cat# 2652; RRID:AB_11178941
anti-Lamin A/C	Cell Signaling	Cat# 2032; RRID:AB_2136278
anti-MSMO1	Novus	Cat# NBP-59450; RRID:AB_2860020
anti-HMGCR	Novus	Cat# NBP2-66888; RRID:AB_2860021
anti-βactin	Sigma	Cat# A1978; RRID:AB_476692
anti-FADS2	Thermo	Cat# PA5-87765; RRID:AB_2804393
anti-ACTA2	Antibodies	Cat# A43414
anti-Ki67	abcam	Cat# ab8191; RRID:AB_306346
anti-rabbit Alexa Fluor 555	Thermo	Cat# A-21428; RRID:AB_2535849
anti-mouse Alexa Fluor 555	Thermo	Cat# A-21422; RRID:AB_2535844
anti-rabbit Alex Fluor 488	Thermo	Cat# A-11034; AB_2576217
Goat anti-rabbit-IgG-HRP	Thermo	Cat# 31460; RRID:AB_228341
Goat anti-mouse-IgG-HRP	Thermo	Cat# 31430; RRID:AB_228307
Chemicals, Peptides, and Recombinant Proteins		
azathioprine	Sigma	Cat# A4638
temozolomide	Sigma	Cat# T2577
FDA-approved Drug Library	Enzo Life Sciences	Cat# BML-2841
NIH clinical collection (446 compounds)	Evotec	NIH clinical collection 1 (https://pubchem.ncbi.nlm.nih.gov/source/NIH%20Clinical%20Collection)
L-glutamine	Gibco	Cat# 25030-081
EGF	R&D systems	Cat# 236-EG
FGF	R&D systems	Cat# 3718-FB
laminin	Sigma	Cat# L2020
fibronectin	Gibco	Cat# 33016-015
Critical Commercial Assays		
CCK8	Dojindo	Cat# CK04

CellTiter-Glo 3D cell viability reagent	Promega	Cat# G9683
EGFR Kinase Enzyme System Analysis Kit	Promega	Cat# V3831
ADP-Glo Kinase Assay Kit	Promega	Cat# V9101
iTRAQ Reagents Multiplex Kit (4plex)	AB SCIEX	Cat# 4352135
CytoX	LPS Solution	Cat# CYT3000
Deposited Data		
Raw and analyzed data (WES, mRNA-seq, microarray)	This paper	GEO: GSE153908
Experimental Models: Cell Lines		
559T	Dr. Do-Hyun Nam	N/A
592T	Dr. Do-Hyun Nam	N/A
626T	Dr. Do-Hyun Nam	N/A
Normal human astrocyte	Lonza	CC-2565
A549	ATCC	CCL-185; RRID:CVCL_0023
592T-Luciferase	This paper	N/A
Experimental Models: Organisms/Strains		
BALB/c Nude mice	Orient Bio Inc. Korea	RRID:IMSR_CRL:194
Oligonucleotides		
MGMT Forward: 5'-CCTGGCTGAATGCCTATTTCCAC-3'	This paper	N/A
MGMT Reverse: 5'-GCAGCTTCCATAACACCTGTCTG-3'	This paper	N/A
SLC3A2 Forward: 5'-TCTTGATTGCGGGGACTAAC -3'	This paper	N/A
SLC3A2 Reverse: 5'-GCCTTGCCTGAGACAAACTC -3'	This paper	N/A
FLT Forward: 5'-AGGCCCTTTTGGATCTTCAT-3'	This paper	N/A
FLT Reverse: 5'-GCTTGAGAGTGAGCCTTTCG-3'	This paper	N/A
LC3A Forward: 5'-CGTCCTGGACAAGACCAAGT-3'	This paper	N/A
LC3A Reverse: 5'-CTCGTCTTTCTCCTGCTCGT-3'	This paper	N/A
GADD45G Forward: 5'-TACGCTGATCCAGGCTTTCT-3'	This paper	N/A
GADD45G Reverse: 5'-AACAGGCTGAGCTTCTCCAA-3'	This paper	N/A
CTSD Forward: 5'-GACACAGGCACTTCCCTCAT-3'	This paper	N/A

CTSD Reverse: 5'-CTCTGGGGACAGCTTGTAGC-3'	This paper	N/A
ALDH3A1 Forward: 5'-GCAGACCTGCACAAGAATGA-3'	This paper	N/A
ALDH3A1 Reverse 5'-GCTCCGAGTGGATGTAGAGC-3'	This paper	N/A
FUT3 Forward: 5'-AGGTGTACCCACAGGCAGAC-3'	This paper	N/A
FUT3 Reverse: 5'-GCGGTAGGACATGGTGAGAT-3'	This paper	N/A
NQO1 Forward: 5'-AAAGGACCCTTCCGGAGTAA-3'	This paper	N/A
NQO1 Reverse: 5'- CCATCCTTCCAGGATTTGAA-3'	This paper	N/A
AOC2 Forward: 5'-GGATAGCAGCTTTGGACTCG-3'	This paper	N/A
AOC2 Reverse: 5'-AGGTAATTGTGGTGCCTTCG-3'	This paper	N/A
ATF4 Forward: 5'-GGGACAGATTGGATGTTGGAGA-3'	This paper	N/A
ATF4 Reverse: 5'-ACCCAACAGGGCATCCAAGT-3'	This paper	N/A
CHOP Forward: 5'-CAGAACCAGCAGAGGTCACA-3'	This paper	N/A
CHOP Reverse 5'-AGCTGTGCCACTTTCCTTTC-3'	This paper	N/A
XBP1 Forward: 5'-TCACCCCTCCAGAACATCTC-3'	This paper	N/A
XBP1 Reverse: 5'-AAAGGGAGGCTGGTAAGGAA-3'	This paper	N/A
NOS2 Forward: 5'-AGGGACAAGCCTACCCCTC-3'	This paper	N/A
NOS2 Reverse: 5'-CTCATCTCCCGTCAGTTGGT-3'	This paper	N/A
ACAT2 Forward: 5'-AAAAGCAGGTTGGTCACTGG-3'	This paper	N/A
ACAT2 Reverse: 5'-CGACTTCTGCCCATTCTCTC-3'	This paper	N/A
LIPG Forward: 5'-TCAACGATGTCTTGGGATCA-3'	This paper	N/A

LIPG Reverse: 5'-TGAAGCGATTGGAGTCAGTG-3'	This paper	N/A
MSMO1 Forward: 5'-GGAATCGTGCTTTTGTGTGA-3'	This paper	N/A
MSMO1 Reverse 5'-AAATCATGATGCCGAGAACC-3'	This paper	N/A
THBS2 Forward: 5'-TCGTGCGCTTTGACTACATC-3'	This paper	N/A
THBS2 Reverse: 5'-GTGCCGTCAATCCAGTAGGT-3'	This paper	N/A
ITGA6 Forward: 5'-GGAGCCCCACAGTATTTTGA-3'	This paper	N/A
ITGA6 Reverse: 5'-TTCCATTTGCAGATCCATGA-3'	This paper	N/A
COL4A1 Forward: 5'-GAAGGGTGATCCAGGTGAGA -3'	This paper	N/A
COL4A1 Reverse: 5'-CACCCTTGTCACCTTTTGGT-3'	This paper	N/A
EPHA2 Forward: 5'-GAGGGCGTCATCTCCAAATA-3'	This paper	N/A
EPHA2 Reverse: 5'-TCAGACACCTTGCAGACCAG-3'	This paper	N/A
EGFR Forward: 5'-TGCGTCTCTTGCCGGAAT-3'	This paper	N/A
EGFR Reverse: 5'-GGCTCACCCTCCAGAAGGTT-3'	This paper	N/A
LDLR Forward: 5'-TACAAGTGGGTCTGCGATGG-3'	This paper	N/A
LDLR Reverse: 5'-TGAAGTCCCCGGATTTGCAG-3'	This paper	N/A
CDC7 Forward: 5'-TCAGCAGTCCACCACAAAAG-3'	This paper	N/A
CDC7 Reverse: 5'-AGGGCTCTCATGTGAAATGG-3'	This paper	N/A
CDC45 Forward: 5'-GCAGGTGAAGCAGAAGTTCC -3'	This paper	N/A

CDC45 Reverse: 5'-AAGACATGGTGGCAAAGACC-3'	This paper	N/A
SKP2 Forward: 5'-CATTTCAGCCCTTTTCGTGT-3'	This paper	N/A
SKP2 Reverse: 5'-GGGCAAATTCAGAGAATCCA-3'	This paper	N/A
ACTA2 Forward: 5'-TTCAATGTCCCAGCCATGTA-3'	This paper	N/A
ACTA2 Reverse: 5'-GAAGGAATAGCCACGCTCAG-3'	This paper	N/A
ACACA Forward: 5'-ACCACCAATGCCAAAGTAGC-3'	This paper	N/A
ACACA Reverse: 5'-CTGCAGGTTCTCAATGCAAA-3'	This paper	N/A
HMGCR Forward: 5'-GTCATTCCAGCCAAGGTTGT -3'	This paper	N/A
HMGCR Reverse: 5'-GGGACCACTTGCTTCCATTA-3'	This paper	N/A
INSIG1 Forward: 5'-TACGCTGATCACGCAGTTTC-3'	This paper	N/A
INSIG1 Reverse: 5'-TCACTATGGGGCTTTTCAGG-3'	This paper	N/A
FADS2 Forward: 5'-ACCTGCCCTACAATCACCAG-3'	This paper	N/A
FADS2 Reverse: 5'-AGGTGATGAAGAACCGGATG-3'	This paper	N/A
Recombinant DNA		
CMV-Luciferase-Puro	This paper	N/A
Software and Algorithms		
GraphPad Prism 8	GraphPad Software	N/A
ImageJ	NIH	N/A
R	N/A	https://www.r-project.org/

BWA	(Li and Durbin, 2009)	http://bio-bwa.sourceforge.net/bwa.shtml, version 0.7.12
SnpEff v4.1g	(Cingolani et al., 2012)	(http://snpeff.sourceforge.net/SnpEff.html
Bowtie2	(Langmead and Salzberg, 2012)	http://bowtie-bio.sourceforge.net/bowtie2/index.shtml
KEGG pathway	(Kanehisa et al., 2012)	https://www.genome.jp/kegg/
Search Tool for the Retrieval of Interacting Genes/Proteins (STRING)	(Szklarczyk et al., 2019)	https://string-db.org/
Other		
Trizol	Invitrogen	Cat# 15596018
ReliaPrep gDNA Tissue Miniprep System	Promega	Cat# A2051

METHOD DETAILS

Cell Culture

559T, 592T, 626T cells were obtained from patients at Samsung Medical Center (Seoul, Republic of Korea) on the basis of an informed consent form approved by the Institutional Review Board (IRB No. 2005-04-001, 2010-04-004). GBM tumor tissues were surgically isolated and mechanically dissected. For single cell purification, enzymatic dissociation was conducted (Joo et al., 2013). Primary GBM cells, U87MG (ATCC), and T98G (ATCC) were maintained in spheroidal suspension in Neurobasal-A medium (Gibco, 10888-022) supplemented with 0.5X B-27 (Gibco, 17504-001), 0.5X N2 (Gibco, 17502-001), L-glutamine (2 mM, Gibco, 25030-081), EGF (100 ng/ml, R&D systems, 236-EG), FGF (100 ng/ml, R&D systems, 3718-FB) and ZellShield (Minerva Biolabs GmbH). To attach GBM to culture dishes, cells were cultured in laminin- (L2020, Sigma) and fibronectin- (33016-015, Gibco) coated culture dishes. U87MG and T98G were maintained in EMEM (ATCC, Cat. No. 30-2003) supplemented with 10% FBS, 1% ZellShield for routine 2D culture. NHA cells were purchased

from Lonza (CC-2565) and cultured in ABM medium (Lonza, CC-3187) supplemented with AGM SingleQuots (CC-4123) and ZellShield (Minerva Biolabs GmbH). A549 cells (ATCC) and HCC-95 (KCLB) were maintained in RPMI 1640 supplemented with 10% FBS, 1% penicillin/streptomycin solution. All cells were routinely tested for mycoplasma.

Antibodies, Reagents and DNA plasmid

Commercially available antibodies used were: anti-SREBP-1 (sc-13551, 1:1000 dilution for IB analysis), anti-LXR (sc-13068, 1:500 dilution for IB analysis), and anti-p27 (sc-528, 1:2500 dilution for IB analysis) from Santa Cruze; anti-LDLR (ab30532, 1:1000 dilution for IB analysis), anti-p62 (ab101266, 1:1000 dilution for IB analysis), anti-FDFT1 (ab195046, 1:1000 dilution for IB analysis), anti-Tubulin (ab176560, 1:2500 dilution for IB analysis), and anti-FOXO1A (ab52857, 1:1000 dilution for IB analysis) from abcam; anti-MGMT (#2739, 1:1000 dilution for IB analysis), anti-EPHA2 (#6997, 1:1000 dilution for IB analysis), anti-EGFR (#2232, 1:1000 dilution for IB analysis), anti-AKT (#4691, 1:1000 dilution for IB analysis), anti-phospho-AKT (#4060, 1:1000 dilution for IB analysis), anti-STAT3 (#9139, 1:1000 dilution for IB analysis), anti-phospho-STAT3 (#9145, 1:1000 dilution for IB analysis), anti-cleaved caspase3 (#9661, 1:1000 dilution for IB analysis), anti-cleaved PARP1 (#5625, 1:1000 dilution for IB analysis), anti-CHOP (#2895, 1:1000 dilution for IB analysis), anti-LC3 (#2775, 1:1000 dilution for IB analysis), anti-CDC7 (#3603, 1:1000 dilution for IB analysis), anti-CDC45 (#11881, 1:1000 dilution for IB analysis), anti-SKP2 (#2652, 1:1000 dilution for IB analysis), and anti-Lamin A/C (#2032, 1:1000 dilution for IB analysis) from Cell Signaling; anti-MSMO1 (NBP-59450, 1:1000 dilution for IB analysis) and anti-HMGCR (NBP2-66888, 1:1000 dilution for IB analysis) from Novus; anti-βactin (A1978, 1:10000 dilution for IB analysis) from Sigma; anti-FADS2 (PA5-87765, 1:1000 dilution for IB analysis) from Thermo; and anti-ACTA2 (A43414, 1:1000 dilution for IB analysis)

from Antibodies. Azathioprine (A4638), temozolomide (T2577), and staurosporine (S5921) were from Sigma. Lapatinib (S2111) was from Selleck Chemicals. EGFR WT expression plasmid was a gift from Matthew Meyerson (Addgene plasmid # 11011).

Preparation of Whole-cell Lysates and Subcellular Fractions

A day after attachment culture dishes, GBM cells were treated with indicated drugs for indicated times. Before collection, all cells were briefly washed with cold PBS. Cells were resuspended in RIPA buffer with freshly added protease inhibitor cocktail (cOmplete, Roche) for whole-cell lysates preparation. After vigorous rocking at 4°C for 30 min, cells were spun by centrifuge, and supernatants (whole-cell lysate) were transferred to a new tube.

For subcellular fractions, cells were lysed in buffer A (10 mM KCl, 10 mM HEPES [pH 7.9], 0.1 mM EGTA, 0.1 mM EDTA, and freshly added PMSF, DTT and protease inhibitors), incubated on ice and treated with 0.5% NP-40, and the then spun by cenrifuge. The supernatant was collected for cytosolic fraction. The pellet was washed twice with buffer A and resuspended in buffer C (400 mM NaCl, 20 mM HEPES [pH 7.9], 1 mM EGTA , 1 mM EDTA, and freshly added PMSF, DTT and protease inhibitors). Pierce BCA protein assay kit (Thermo, 23227) was used for protein quantification.

SDS-PAGE and Immunoblot Analysis

4-20% Mini-PROTEAN TGX Precast Protein Gels (Bio-rad, #459-1096) were used for SDS-PAGE. After transfering to PVDF membranes, membranes were incubated with blocking solution (5 % skim milk or BSA in TBS-T) and then incubated in primary antibodies diluted in 3% BSA in TBS-T. After 6 washes in TBS-T, membranes were incubated in appropriate secondary HRP-

conjugated antibodies (Thermo, 1:5000 dilution in blocking solutions). After 6 washes in TBS-T, membranes were incubated in ECL substrate (Pierce, 34096) and imaged by LAS3000 (Fujifilm) or WSE-6200H (ATTO).

2D and 3D Cell Viability Assay

For the 2D cell assay, 10,000 cells per well were seeded in complete media on laminin- and fibronectin-coated 96-well transparent bottom plates. The next day drugs were added and cells incubated for an additional indicated time after adding indicated concentrations of drugs. CCK8 (Dojindo) was added, and O.D. values were measured. Values were normalized to the DMSO control, and the IC50 was calculated using GraphPad Prism 8. For the 3D assay, 559T, U87MG, T98G (5,000 cells per well) and 592T (3,000 cells per well) cells were seeded in complete media on ultra low attachment 96-well plates (Corning, 4520). To establish solid and uniform spheres, plates were incubated for 3 days. Drugs were then added and cells were incubated for indicated time. The CellTiter-Glo 3D cell viability reagent (Promega, G9683) was added, and luciferase values were measured. Values were normalized to the DMSO control, and the IC50 was calculated using GraphPad Prism 8.

Transmission Electron Microscopy (TEM)

GBM were attached to culture dishes as described and the next day treated with azathioprine for indicated times. Cells were then fixed 24 hours in PBS containing 2% paraformaldehyde (EM grade) and 2% glutaraldehyde (EM grade) at 4°C and post-fixed with 2% Osmium tetroxide for 1 hour at room temperature. After washing, cells were dehydrated through an ethanol series (20 min per step) starting from 50% and ending with 100%. Cells were incubated with progressively concentrated propylene oxide dissolved in ethanol. Then, cells were infiltrated with an increasing

concentration of Epon 812 resin. Samples were baked in a 60°C oven for 48 hours and then sectioned using an Ultra microtome (70 nm thickness, Leica EM UC7). Sections were viewed with TEM (JEM-2100F, JOEL) at Korean Basic Science Institute Chuncheon Center, Republic of Korea.

RNA Preparation and Quantitative RT-PCR

Total RNA was prepared using TRIzol (Invitrogen). For cDNA generation, RNA was reverse transcribed with SuPrimeScript Reverse Transcriptase (GeNetBio). cDNAs were mixed with TOPreal™ qPCR 2X PreMIX SYBR Green with low ROX (Enzynomics, RT500M) and gene-specific primers for PCR. mRNA abundance was assessed using the ABI 7500F system or the Qiagen Rotor-Gene Q system. The following primers were used:

MGMT Forward 5'- CCTGGCTGAATGCCTATTTCCAC -3',
MGMT Reverse 5'- GCAGCTTCCATAACACCTGTCTG -3',
SLC3A2 Forward 5'- TCTTGATTGCGGGGACTAAC -3',
SLC3A2 Reverse 5'- GCCTTGCCTGAGACAAACTC -3',
FLT Forward 5'- AGGCCCTTTTGGATCTTCAT -3',
FLT Reverse 5'- GCTTGAGAGTGAGCCTTTCG -3',
LC3A Forward 5'- CGTCCTGGACAAGACCAAGT -3',
LC3A Reverse 5'- CTCGTCTTTCTCCTGCTCGT -3',
GADD45G Forward 5'- TACGCTGATCCAGGCTTTCT -3',
GADD45G Reverse 5'- AACAGGCTGAGCTTCTCCAA -3',
CTSD Forward 5'- GACACAGGCACTTCCCTCAT -3',
CTSD Reverse 5'- CTCTGGGGACAGCTTGTAGC -3',
ALDH3A1 Forward 5'- GCAGACCTGCACAAGAATGA -3',
ALDH3A1 Reverse 5'- GCTCCGAGTGGATGTAGAGC -3',
FUT3 Forward 5'- AGGTGTACCCACAGGCAGAC -3',
FUT3 Reverse 5'- GCGGTAGGACATGGTGAGAT -3',

NQO1 Forward 5’- AAAGGACCCTTCCGGAGTAA -3’,

NQO1 Reverse 5’- CCATCCTTCCAGGATTTGAA -3’,

AOC2 Forward 5’- GGATAGCAGCTTTGGACTCG -3’,

AOC2 Reverse 5’- AGGTAATTGTGGTGCCTTCG -3’,

ATF4 Forward 5’- GGGACAGATTGGATGTTGGAGA -3’,

ATF4 Reverse 5’- ACCCAACAGGGCATCCAAGT -3’,

CHOP Forward 5’- CAGAACCAGCAGAGGTCACA -3’,

CHOP Reverse 5’- AGCTGTGCCACTTTCCTTTC -3’,

XBP1 Forward 5’- TCACCCCTCCAGAACATCTC -3’,

XBP1 Reverse 5’- AAAGGGAGGCTGGTAAGGAA -3’,

NOS2 Forward 5’- AGGGACAAGCCTACCCCTC -3’,

NOS2 Reverse 5’- CTCATCTCCCGTCAGTTGGT -3’,

ACAT2 Forward 5’- AAAAGCAGGTTGGTCACTGG -3’,

ACAT2 Reverse 5’- CGACTTCTGCCCATTCTCTC -3’,

LIPG Forward 5’- TCAACGATGTCTTGGGATCA -3’,

LIPG Reverse 5’- TGAAGCGATTGGAGTCAGTG -3’,

MSMO1 Forward 5’- GGAATCGTGCTTTTGTGTGA -3’,

MSMO1 Reverse 5’- AAATCATGATGCCGAGAACC -3’,

THBS2 Forward 5’- TCGTGCGCTTTGACTACATC -3’,

THBS2 Reverse 5’- GTGCCGTCAATCCAGTAGGT -3’,

ITGA6 Forward 5’- GGAGCCCCACAGTATTTTGA -3’,

ITGA6 Reverse 5’- TTCCATTTGCAGATCCATGA -3’,

COL4A1 Forward 5’- GAAGGGTGATCCAGGTGAGA -3’,

COL4A1 Reverse 5’- CACCCTTGTCACCTTTTGGT -3’,

EPHA2 Forward 5’- GAGGGCGTCATCTCCAAATA -3’,

EPHA2 Reverse 5’- TCAGACACCTTGCAGACCAG -3’,

EGFR Forward 5’- TGCGTCTCTTGCCGGAAT -3’,

EGFR Reverse 5’- GGCTCACCCTCCAGAAGGTT -3’,

LDLR Forward 5’- TACAAGTGGGTCTGCGATGG -3’,

LDLR Reverse 5'- TGAAGTCCCCGGATTTGCAG -3',
CDC7 Forward 5'- TCAGCAGTCCACCACAAAAG -3',
CDC7 Reverse 5'- AGGGCTCTCATGTGAAATGG -3',
CDC45 Forward 5'- GCAGGTGAAGCAGAAGTTCC -3',
CDC45 Reverse 5'- AAGACATGGTGGCAAAGACC -3',
SKP2 Forward 5'- CATTTCAGCCCTTTTCGTGT -3',
SKP2 Reverse 5'- GGGCAAATTCAGAGAATCCA -3',
ACTA2 Forward 5'- TTCAATGTCCCAGCCATGTA -3',
ACTA2 Reverse 5'- GAAGGAATAGCCACGCTCAG -3',
ACACA Forward 5'- ACCACCAATGCCAAAGTAGC -3',
ACACA Reverse 5'- CTGCAGGTTCTCAATGCAAA -3',
HMGCR Forward 5'- GTCATTCCAGCCAAGGTTGT -3',
HMGCR Reverse 5'- GGGACCACTTGCTTCCATTA -3',
INSIG1 Forward 5'- TACGCTGATCACGCAGTTTC -3',
INSIG1 Reverse 5'- TCACTATGGGGCTTTTCAGG -3',
FADS2 Forward 5'- ACCTGCCCTACAATCACCAG -3',
FADS2 Reverse 5'- AGGTGATGAAGAACCGGATG -3'.

Whole Exome Sequencing

559T or 592T cell genomic DNA was prepared using a ReliaPrep gDNA kit (Promega, A2051). Library preparation, sequencing, and basic analysis were conducted by MACROGEN Company (Republic of Korea). Samples were prepared according to an Agilent SureSelect Target Enrichment Kit preparation guide. Libraries were sequenced with the Illumina platform sequencer. Paired-end sequences produced by the HiSeq Instrument were mapped to the human genome (*hg19*, original GRCh37 from NCBI, Feb. 2009), without unordered sequences and alternate haplotypes, using the mapping program 'BWA' (http://bio-bwa.sourceforge.net/bwa.shtml, version 0.7.12) to generate a mapping result file in BAM format using 'BWA-MEM'. We then applied programs packaged in Picard-tools (ver.1.130) to remove PCR duplicates by reducing reads identically

matched to a single one, using MarkDuplicates.jar. A local realignment process was performed to consume BAM files and locally realign reads. Base quality score recalibration (BQSR) and local realignment around indels were performed using a Genome Analysis Toolkit. Variant genotyping for each sample was performed using Haplotype Caller of GATK (https://www.broadinstitute.org/gatk/). At this stage, SNP and short indels candidates were detected at nucleotide resolution. Those were annotated by the program SnpEff v4.1g (http://snpeff.sourceforge.net/SnpEff.html) to vcf file format, filtering with dbSNP for version, and SNPs from the 1000 genome project. Then, an in-house program and SnpEff was applied to filter additional databases, including ESP6500, dbNSFP2.9, ClinVar. We gathered all per-sample GVCFs and passed them all together to a joint genotyping tool, GenotypeGVCFs for advanced analysis, An enrichment test based on the KEGG Pathway (Kyoto Encyclopedia of Genes and Genomes (Kanehisa et al., 2012) was conducted using genes annotated from variants in the VCF.

mRNA-sequencing

The day after GBM were attached to culture dishes, cells were treated 48 hours with 10 μM azathioprine or DMSO vehicle. Total RNA was isolated using TRIzol (Invitrogen). Library preparation, sequencing, and basic analysis were conducted by MACROGEN Company (Republic of Korea). The cDNA libraries were constructed with the TruSeq Stranded mRNA LT Sample Prep Kit. Sequencing was performed by Illumina NovaSeq 6000. Libraries were quantified using qPCR and qualified using an Agilent Technologies 2100 Bioanalyzer. We preprocessed raw reads to remove low quality and adapter sequences before analysis and aligned processed reads to the *Homo sapiens (hg19)* using HISAT v2.3.4.1 (Kim et al., 2015). The reference genome *Homo sapiens (hg19)* sequence and annotation data were downloaded from NCBI. Transcript assembly of known transcripts was processed by StringTie v1.3.4d (Pertea et al., 2016; Pertea et al., 2015),

and transcript and gene abundance was calculated as read counts or FPKM values (Fragments Per Kilobase of exon per Million fragments mapped) per sample. Expression profiles were used for DEGs (Differentially Expressed Genes) analysis. Relative gene abundance was measured in FPKM using StringTie. Genes with one more than zero FPKM values in samples were excluded and one was added to each FPKM value of filtered genes to facilitate log2 transformation. Filtered data were log2-transformed and subjected to quantile normalization. Statistical significance of DEGs was determined by an independent t-test. False discovery rate (FDR) was controlled by adjusting p-values using Benjamini-Hochberg algorithm. Hierarchical clustering analysis was performed using complete linkage and Euclidean distance to display expression patterns of DEGs which satisfied the criteria $|\text{fold change}| \geq 2$ and raw $p < 0.05$. KEGG pathway analysis for DEGs was performed based on the database (https://www.genome.jp/kegg/). All data analysis and visualization of DEGs was conducted using R 3.6.0 (www.r-project.org).

Sample Preparation for Proteomic Analysis

The day after GBM were attached to culture dishes, cells were treated 48 hours with 10 μM azathioprine, washed with cold PBS and collected. Cell pellets were resuspended in lysis buffer (75 mM NaCl, 8 M urea, 50 mM Tris-HCl [pH 8.0], and protease inhibitors). The lysate was sonicated and centrifuged to remove debris and protein concentration determined using a bicinchoninic acid (BCA) assay. An equal amount of protein was reduced with 10 mM dithiothreitol (DTT) for 2 hours at 37°C and alkylated with 20 mM iodoacetamide (IAA) for 30 min at room temperature in dark. The remaining IAA was quenched with 20 mM L-cysteine for 30 min at room temperature. After adding three volumes of 50 mM ammonium bicarbonate buffer, proteins were digested with trypsin (1:50, w/w) at 37°C. Following digestion for 18 hours, peptide mixtures were acidified with 1% formic acid (v/v) to stop the reaction and desalted on OASIS

HLB cartridges (Waters, Milford, MA, USA). Eluted peptide samples were completely dried in a vacuum concentrator.

iTRAQ labeling of peptides from 559T and 592T cells was performed using a 4-*plex iTRAQ reagent kit* (AB SCIEX). Briefly, dried peptides were dissolved in 30 µl 0.5 M triethylammonium bicarbonate (TEAB) buffer and labeled with 4-plex iTRAQ reagents as follows: 114 isobaric tags for 559T cells and 115 isobaric tags for 559T cells treated with azathioprine. After a 2 hour incubation at room temperature, reaction for labeling was stopped by adding of 1% formic acid (v/v). Labeled peptides were pooled, desalted with OASIS HLB cartridges and dried in a vacuum concentrator. For LC-MS/MS analysis, resulting peptides were reconstituted in 0.1% formic acid. The dataset was obtained from two biological replicates with two technical replicate -LC runs for each. iTRAQ labeling of peptides from 592T cells was also conducted as described above (114 isobaric tags for 592T cells and 115 isobaric tags for 592T cells treated with azathioprine).

Nanoflow Liquid Chromatography-Tandem Mass Spectrometry (nLC-MS/MS) Analysis

Samples were analyzed on a capillary LC system (Agilent Technologies, Waldbronn, Germany) coupled to Q-Exactive FT orbitrap-mass spectrometer (Thermo Fisher Scientific) equipped with a nanoelectrospray source. For online two-dimensional (2D)-nLC operation, biphasic trap columns (40 mm long, 200-µm I.D) were in-house packed with 5 mm of reverse-phase (RP) C18 resin (5 µm-200 Å) followed by 15 mm of SCX resin (5 µm-200 Å), as described (Kang et al., 2005). Peptides were injected onto the SCX phase of the column and fractionated with 12-step salt gradients (0, 20, 22, 24, 26, 28, 30, 35, 40, 60, 100 and 1000 mM ammonium bicarbonate buffer containing 0.1% formic acid). Eluted peptides at each step were directly bound to the RP phase of the column, followed by RP gradients_at a flow rate 200 nL/min for 120 min. Peptides were separated on a RP analytical column (150 mm long, 75 µm I.D) packed with C18 resin (3 µm-100

Å). A gradient was generated by buffer A (0.1% FA in water) and B (2% water/0.1% FA in acetonitrile).

The mass spectrometer was operated in data-dependent mode. Full-scan MS spectra were acquired at a resolution of 70,000 with automatic gain control (AGC) target value of 3×10^6, and within mass ranges of *m/z* 300-1800. The 12 most intensive precursor ions from the MS scan were selected for high-energy collision dissociation (HCD). MS/MS scans were performed at a resolution of 35,000 with a first fixed mass at 100 *m/z*. Precursor ions with single or unassigned charge state were rejected from fragmentation. Dynamic exclusion was allowed for a duration of 30 s.

Proteomic Data Analysis

MS/MS raw data files were searched with MaxQuant software (version 1.6.0.1) against the Uniprot *Homo sapiens* database (release Apr 21, 2019). Search parameters were as follows: two missed trypsin cleavages were allowed; precursor ion mass tolerance was 4.5 ppm; fragment ion mass tolerance was 20 ppm; carbamidomethylation (C), iTRAQ4plex (N-term) and iTRAQ4plex (K) were set as fixed modifications; oxidation (M) and acetylation (N-term) were set as variable modifications; and the FDR was set to 0.01 at peptide and protein levels. Included for identification were only protein groups with at least two unique peptides per protein. Potential contaminants and reverse hits were removed. For further statistical analysis, only protein groups quantified in at least three of the four replicates were considered. Data processing and statistical analysis was conducted using Perseus software (version 1.5.8.5). iTRAQ ratios (115/114) were $\log_2$ transformed, normalized to the median and subjected to Student's t-test. Gene Ontology (GO) enrichment terms were analyzed by STRING. Enrichment analysis of the reactome pathway was performed using R/Bioconductor package ReactomePA (version 1.30.0) (Yu and He, 2016).

For integration analysis of transcriptomic and proteomic data, protein-transcript pairs were identified (p-value < 0.05 at transcriptomic and proteomic levels; 665 pairs for 559T cells and 415 for 592T cells). The Pearson correlation coefficient (*R*) and p-values were calculated using Perseus software. PPI network analysis (medium confidence score > 0.4.) and reactome pathway enrichment analysis of proteins commonly regulated at transcriptomic and proteomic levels were performed using STRING database.

High Throughput Screening

An FDA-approved Drug Library (640 drugs) was purchased from Enzo Life Sciences and the NIH clinical collection (446 compounds) from Evotec. Biomek FX (Beckman Coulter) was used to treat cells with diluted library compounds to achieve final concentrations. Vehicle (0.1 % DMSO in media) served as negative control, while doxorubicin served as positive. GBM cells were seeded at 1,500 cells per well in laminin-coated 384-well plate, and A549 cells were seeded at 1,000 cells per well in 384-well plate. After 24 hours of incubation, cells were treated with compounds and incubated for 72 hours. CytoX (WST-1 reagent, LPS Solution) was added and cells were further incubated for 4 hours at 37°C. Absorbance at 450 nm was assayed on Envision (PerkinElmer). Dose-response curves were constructed in triplicate, and the IC50 value was calculated by nonlinear regression analysis (GraphPad Prism Program, CA, USA).

Microarray Experiments

Total RNA (250 ng) obtained from GBM cells was used to synthesize biotin-labeled RNA. After fragmentation, biotin-labeled cRNAs were hybridized 16 hours at 45°C, according to standard Affymetrix protocols. The Human Genome Array GeneChip containing 49,395 probes and 19,395 genes was used in triplicate for each of three independent sets (559T, 592T, NHA cells) on separate

array chips. An Affymetrix GeneChip Scanner 3000 7G was used to scan chips and data were analyzed using the Affymetrix Expression Console and summarized using the probe logarithmic intensity error algorithm. Background correction and normalization was conducted using Perfect Match and Sketch-Quantile, respectively. As reported (Chae et al., 2013), an integrative statistical test was used to identify DEGs. For each probe set, p values from Student's t-test and $\log_2$-median-ratio test were computed and combined. In brief, the Gaussian kernel density estimation method generated empirical null distributions and log2-median-ratios from random permutations of samples between groups (Bowman and Azzalini, 1997). For each probe set, p values from the two tests were obtained by a two-tailed test with empirical distributions and combined into an overall p value using Stouffer's method (Hwang et al., 2005).

***In Vivo* Xenograft Mouse Model**

All animal experimental procedures were approved by the Institutional Animal Care and Use Committee (IACUC) of Korea Research Institute of Chemistry Technology (KRICT). For xenograft experiments (KRICT ID: 6B-M14), 7 week old female athymic (nu/nu) mice (Orient Bio Inc. Korea) were anesthetized with an Avertin solution (240 mg/kg) and placed in a sterotaxic apparatus. A midline incision was made using aseptic surgical techniques and the scalp opened to expose frontal and temporalis bones. A burr hole was made throught the skull at 1 mm posterior to bregma and 3 mm right of the midline without breaking the dura. A 1/32 inch electric drill needle was inserted 5 mm ventral to the dura and retracted 0.5 mm (for injection), and then patient-derived proneural GBM cells were implanted sterotaxically at an infusion rate of 1 ul/min using a microapillary tube needle. A total 5 X 10^5 592T-Luc cells per mouse was administered. The needle was held in place 2-3 minutes to allow pressure equilibration within the cranial vault and then

removed slowly, and the hole immediately sealed with sterile bone-was to prevent leakage. Animals recovered from anesthesia and were returned to the anumal facility. Mice were monitored daily for neurologic changes, and tumor growth was tracked using NightOWL LB 983 *in vivo* Imaging System (Berthold Technologies, Germany). Tumors were first identified starting at 2 weeks after injection and mice were divided into vehicle and treatment groups containing lesions of similar initial size. Animals in various treatment groups were orally administered 65 mg/kg TMZ daily for 5 days, 5 mg/kg azathioprine daily for 25 days, or a combination of azathioprine (5 mg/kg, daily for 25 days) and TMZ (65 mg/kg, daily for first 5 days). *In vivo* luciferase activity was reported as photons per second. Tumors from xenograft mice were fixed with 4% paraformaldehyde (PFA) and paraffin-embedded immediately after mice were euthanized.

For survival experiments, 7 week old female mice were used in the experiment and a total of 2×10^5 559T cells were injected per mouse. Animals were orally administered 65 mg/kg TMZ daily for the first 5 days from the 17^{th} day after tumor cell implantation. Animals were exposed to 2 Gy of radiation daily for the first 5 days from the 17^{th} day after tumor cell implantation. Azathioprine (20 mg/kg) was orally administered daily from the 11^{th} day after tumor cell implantation. Animals were monitored every day.

Immunohistochemistry (IHC)

Paraffin-embedded brain tissues from xenograft mice were trimmed and sectioned for histological analysis. Tumor tissues were cut into 4 μm sections and incubated with anti-cleaved caspase3 (Cell Signaling, #9661, 1:500 dilution for IHC analysis), anti-cleaved PARP (Cell Signaling, #5625, 1:500 dilution for IHC analysis), anti-Ki67 (Abcam, ab8191, 1:500 dilution for IHC analysis), anti-MSMO1 (Novus, NBP-59450, 1:300 dilution for IHC analysis), anti-FADS2 (Invitrogen,

PA5-87765, 1:300 dilution for IHC analysis), and anti-FDFT1 (Abcam, ab195046, 1:300 dilution for IHC analysis) antibodies for overnight. After 3 washes, tissues were incubated with anti-mouse Alexa Fluor 555-, anti-rabbit Alexa Fluor 555-, or anti-rabbit Alex Fluor 488-conjugated IgG (Thermo Scientific) for 1 hour at room temperature. Samples were then mounted and imaged using a LSM700 confocal microscope (Carl Zeiss). Fluorescent intensity was assessed using ImageJ software.

EGFR kinase enzymatic assay

The effects of drugs on inhibition of EGFR were evaluated using EGFR Kinase Enzyme System Analysis Kit (Promega, #V3831) and ADP-Glo Kinase Assay Kit (Promega #V9101) according to the manufacturer's instruction. Reactions and detections were performed in 384-white well plate (Greiner #784075). EGFR recombinant proteins (10ng), substrate (0.2 μg), ATP (5 μM), and indicated drugs were mixed in EGFR kinase buffer (20 mM MgCl2, 2 mM MnCl2, 40 mM Tris [pH 7.5], 0.1 mg/ml BSA, and 50 μM DTT) and incubated for 1 hour at room temperature. Then 5 μl of ADP-Glo reagent was added and incubated for 40 minutes at room temperature. 10 μl of kinase detection reagent was added and incubated for 30 minutes at room temperature. Luminescence was measured with 1 sec/well integration time using EnVision instrument.

Supplemental References

Bowman, A.W., and Azzalini, A. (1997). Applied smoothing techniques for data analysis: the kernel approach with S-Plus illustrations, Vol 18 (OUP Oxford).

Chae, S., Ahn, B.Y., Byun, K., Cho, Y.M., Yu, M.H., Lee, B., Hwang, D., and Park, K.S. (2013). A systems approach for decoding mitochondrial retrograde signaling pathways. Sci Signal *6*, rs4, doi:10.1126/scisignal.2003266.

Cingolani, P., Platts, A., Wang le, L., Coon, M., Nguyen, T., Wang, L., Land, S.J., Lu, X., and Ruden, D.M. (2012). A program for annotating and predicting the effects of single nucleotide polymorphisms, SnpEff: SNPs in the genome of Drosophila melanogaster strain w1118; iso-2; iso-3. Fly (Austin) *6*, 80-92, doi:10.4161/fly.19695.

Hwang, D., Rust, A.G., Ramsey, S., Smith, J.J., Leslie, D.M., Weston, A.D., De Atauri, P., Aitchison, J.D., Hood, L., and Siegel, A.F. (2005). A data integration methodology for systems biology. PNAS *102*, 17296-17301.

Joo, K.M., Kim, J., Jin, J., Kim, M., Seol, H.J., Muradov, J., Yang, H., Choi, Y.L., Park, W.Y., Kong, D.S.*, et al.* (2013). Patient-specific orthotopic glioblastoma xenograft models recapitulate the histopathology and biology of human glioblastomas in situ. Cell Rep *3*, 260-273, doi:10.1016/j.celrep.2012.12.013.

Kanehisa, M., Goto, S., Sato, Y., Furumichi, M., and Tanabe, M. (2012). KEGG for integration and interpretation of large-scale molecular data sets. Nucleic Acids Res *40*, D109-114, doi:10.1093/nar/gkr988.

Kang, D., Nam, H., Kim, Y.S., and Moon, M.H. (2005). Dual-purpose sample trap for on-line strong cation-exchange chromatography/reversed-phase liquid chromatography/tandem mass spectrometry for shotgun proteomics. Application to the human Jurkat T-cell proteome. J

Chromatogr A *1070*, 193-200, doi:10.1016/j.chroma.2005.02.058.

Kim, D., Langmead, B., and Salzberg, S.L. (2015). HISAT: a fast spliced aligner with low memory requirements. Nat Methods *12*, 357-360, doi:10.1038/nmeth.3317.

Langmead, B., and Salzberg, S.L. (2012). Fast gapped-read alignment with Bowtie 2. Nat Methods *9*, 357-359, doi:10.1038/nmeth.1923.

Li, H., and Durbin, R. (2009). Fast and accurate short read alignment with Burrows-Wheeler transform. Bioinformatics *25*, 1754-1760, doi:10.1093/bioinformatics/btp324.

Pertea, M., Kim, D., Pertea, G.M., Leek, J.T., and Salzberg, S.L. (2016). Transcript-level expression analysis of RNA-seq experiments with HISAT, StringTie and Ballgown. Nat Protoc *11*, 1650-1667, doi:10.1038/nprot.2016.095.

Pertea, M., Pertea, G.M., Antonescu, C.M., Chang, T.C., Mendell, J.T., and Salzberg, S.L. (2015). StringTie enables improved reconstruction of a transcriptome from RNA-seq reads. Nat Biotechnol *33*, 290-295, doi:10.1038/nbt.3122.

Szklarczyk, D., Gable, A.L., Lyon, D., Junge, A., Wyder, S., Huerta-Cepas, J., Simonovic, M., Doncheva, N.T., Morris, J.H., Bork, P.*, et al.* (2019). STRING v11: protein-protein association networks with increased coverage, supporting functional discovery in genome-wide experimental datasets. Nucleic Acids Res *47*, D607-D613, doi:10.1093/nar/gky1131.

Yu, G., and He, Q.Y. (2016). ReactomePA: an R/Bioconductor package for reactome pathway analysis and visualization. Mol Biosyst *12*, 477-479, doi:10.1039/c5mb00663e.